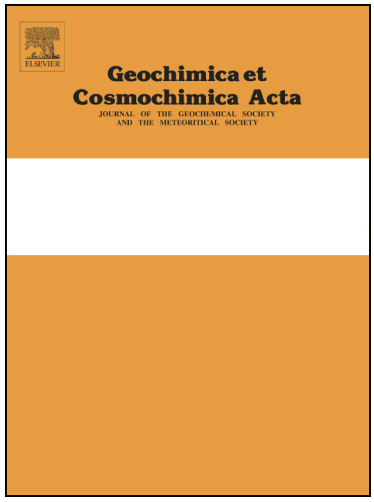


# Influence of surface passivation and water content on mineral reactions in unsaturated porous media: Implications for brucite carbonation and $CO_2$ sequestration

Anna L. Harrison, Gregory M. Dipple, Ian M. Power, K. Ulrich Mayer

PII: S0016-7037(14)00628-0
DOI: http://dx.doi.org/10.1016/j.gca.2014.10.020
Reference: GCA 9027

To appear in: *Geochimica et Cosmochimica Acta*

Received Date: 24 July 2014
Accepted Date: 17 October 2014

Please cite this article as: Harrison, A.L., Dipple, G.M., Power, I.M., Ulrich Mayer, K., Influence of surface passivation and water content on mineral reactions in unsaturated porous media: Implications for brucite carbonation and $CO_2$ sequestration, *Geochimica et Cosmochimica Acta* (2014), doi: http://dx.doi.org/10.1016/j.gca.2014.10.020

# Influence of surface passivation and water content on mineral reactions in unsaturated porous media: Implications for brucite carbonation and $CO_2$ sequestration

Anna L. Harrison*, Gregory M. Dipple, Ian M. Power, and K. Ulrich Mayer

Mineral Deposit Research Unit, Department of Earth, Ocean and Atmospheric Sciences, The University of British Columbia, 2207 Main Mall, Vancouver, British Columbia V6T 1Z4, Canada. ALH* – aharriso@eos.ubc.ca; GMD – gdipple@eos.ubc.ca; IMP – ipower@eos.ubc.ca; KUM – umayer@eos.ubc.ca.

*Corresponding author (phone: 1 604 822 2449; fax: 1 604 822 6088; e-mail: aharriso@eos.ubc.ca).

**Abstract**

The evolution of mineral reactive surface area is an important control on the progress of carbon mineralization reactions that sequester anthropogenic $CO_2$. Dry conditions in unsaturated porous media and the passivation of reactive surface area by secondary phase precipitation complicate predictions of reactive surface during carbon mineralization reactions. Unsaturated brucite [$Mg(OH)_2$] bearing column experiments were used to evaluate the effects of water saturation and hydrous Mg-carbonate precipitation on reaction of brucite with 10% $CO_2$ gas streams at ambient conditions. We demonstrate that a lack of available water severely limits reaction progress largely due to the requirement of water as a reactant to form hydrated Mg-carbonates. The precipitation of a poorly crystalline carbonate phase in the early stages of the reaction does not significantly hinder brucite dissolution, as the carbonate coating remains sufficiently permeable. It is postulated that the conversion of this phase to substantially less porous, crystalline nesquehonite [$MgCO_3 \cdot 3H_2O$] results in passivation of the brucite surface. Although a mechanistic model describing the passivating effect of nesquehonite remains elusive, reactive transport modelling using MIN3P-DUSTY confirms that conventional geometric surface area update models do not adequately reproduce observed reaction progress during brucite carbonation, while an empirically based model accounting for surface passivation is able to capture the transient evolution of $CO_2$ uptake. Both water limits and surface passivation effects may limit the efficiency of $CO_2$ sequestration efforts that rely on the conversion of mafic and ultramafic rock to carbonate minerals.

## 1. Introduction

The evolution of mineral reactive surface area during dissolution-precipitation reactions is an important control on long-term reaction rates in both natural and disturbed environments (White and Brantley, 2003). Mineral dissolution reactions require that mineral surfaces be exposed to a reactive fluid, a criterion that is not always met in porous media. Dry conditions in unsaturated media may leave mineral surfaces insufficiently wetted for dissolution-precipitation reactions to occur, and precipitation of secondary phases at the surface of dissolving phases and within pores may occlude and passivate reactive surfaces. Understanding the effects of water scarcity and secondary precipitates on reactive surface areas of dissolving minerals is important for many areas of research in the Earth sciences, such as nutrient and element cycling, water quality, and $CO_2$ sequestration. The reaction of silicate and hydroxide minerals, such as brucite [$Mg(OH)_2$], with $CO_2$ to form carbonate minerals represents a model system to study these effects due to the coupled nature of the reactions and the extensive reaction progress that can be achieved on an experimental time scale (e.g., Daval et al., 2009a; Assima et al., 2013a; Power et al., 2013a and references therein). Such carbon mineralization reactions are currently under investigation due to their potential application as $CO_2$ sequestration technologies to help offset anthropogenic greenhouse gas emissions (Seifritz, 1990; Lackner et al., 1995; Lackner et al., 1997; Lackner, 2003). These technologies involve injection of $CO_2$-rich fluids or gases into subsurface mafic and ultramafic formations (McGrail et al., 2006; Kelemen and Matter, 2008; Gislason et al., 2010; Van Pham et al., 2012; Gislason and Oelkers, 2014), *ex situ* acceleration in industrial reactors (Gerdemann et al., 2007; Power et al., 2013a), and reaction of Mg and

Ca-rich industrial wastes, such as mine tailings (Pronost et al., 2011; Bobicki et al., 2012; Pronost et al., 2012; Oskierski et al., 2013; Power et al., 2013a; Power et al., 2014a; Assima et al., 2014; Wilson et al., 2014). Similar reactions occur in natural environments during weathering and carbonation of ultramafic rock (e.g., Kelemen and Matter, 2008; Boschi et al., 2009; Power et al., 2014b). Prediction of reaction progress and the fate of $CO_2$ in these and other environments requires accurate representation of the evolution of reactive surface area.

Numerous studies have endeavored to determine the effect of surface coatings on mineral dissolution rates, with conflicting results (c.f., Hodson, 2003; Park and Fan, 2004; Cubillas et al., 2005; Béarat et al., 2006; Lekakh et al., 2008; Andreani et al., 2009; Huntzinger et al., 2009; Daval et al., 2009a; Daval et al., 2009b; Daval et al., 2011; Stockmann et al., 2011; Stockmann et al., 2013). For example, Stockmann et al. (2011, 2013) report no inhibitory effects of calcite precipitation on the dissolution of basaltic glass or diopside. Yet, several studies report inhibited dissolution of serpentine and olivine due to formation of a silica-rich layer at the mineral surface (Park and Fan, 2004; Béarat et al., 2006; Andreani et al., 2009; Daval et al., 2011; Sissmann et al., 2014; Johnson et al., 2014), and Daval et al. (2009a) documented passivation of wollastonite via calcite precipitation. Similarly, Hövelmann et al. (2012a) suggest that precipitation of magnesite during olivine carbonation clogs pores and limits reaction progress, although Lafay et al. (2014) did not observe passivation during carbonation and serpentinization of olivine. Yet, the passivating effect of Mg-carbonates alone may be difficult to assess during silicate carbonation due to the concomitant formation of potentially passivating Si-bearing phases (King et al., 2010). Moreover, a multitude of metastable Mg-carbonate minerals are known to form during carbon mineralization reactions (Hänchen et al., 2008;

Power et al., 2009; Wilson et al., 2009; Beinlich and Austrheim, 2012; Power et al., 2013a). Differences in structure amongst these Mg-carbonates and between Mg- and Ca-carbonates means that their passivating effects are likely highly variable, and may differ from the Ca-carbonates studied previously. The formation of hydrous Mg-carbonates is favoured over precipitation of the anhydrous Mg-carbonate, magnesite [$MgCO_3$] at low temperature (e.g., Hänchen et al., 2008); hence the precipitation of secondary carbonates is accompanied by a loss of pore water due to its incorporation in the mineral structure. The initial volume of water available may restrict the mass of $CO_2$ that can be stored (i.e., the reaction progress) based on the stoichiometry of the hydrated phase (e.g., Schaef et al., 2011; Van Pham et al., 2012). For example, the extent of carbonation of chrysotile mining residues at ambient conditions as well as reaction of brucite and several silicates with wet supercritical $CO_2$ is limited under low water conditions (Loring et al., 2011; Schaef et al., 2011; Schaef et al., 2013; Assima et al., 2013a; Miller et al., 2013). Evaluation of the passivating effects of hydrated Mg-carbonates is therefore complicated by the concurrent loss of pore water.

In this study, we investigate the controls on brucite [$Mg(OH)_2$] carbonation in unsaturated column experiments supplied with 10% $CO_2$ gas. These experiments provide simplified representations of carbon mineralization reactions in partially water saturated porous media, such as the unsaturated zone in natural systems, or disturbed or industrial environments (e.g., mine tailings and urban soils; Washbourne et al., 2012; Wilson et al., 2014). The objective of this study was to evaluate the effect of water saturation and precipitation of hydrous Mg-carbonates at the brucite surface on reaction progress. Because our experiments investigated carbonation of a silica-free mineral, we can assess

the effect of Mg-carbonate precipitates and their different morphologies on the extent of passivation, without the complication of silica layer formation. In addition, experiments of varying water saturation were conducted in order to distinguish between surface passivation-limited and water-limited reaction. The passivating effect of surface coatings has mainly been assessed in fluid dominated stirred reactors as opposed to the mineral dominated column reactors as employed in this study. Passivating effects may differ in these environments due to the limited pore volumes in which secondary phases can form, the relative scarcity of water, and the lack of abrasion that could loosen precipitates in a stirred reactor. The reactive transport model, MIN3P-DUSTY (Mayer et al., 2002; Molins and Mayer, 2007) is applied to help elucidate the processes governing carbonation and to aid in the development of improved modeling capabilities to capture the evolution of reactive surface area during coupled dissolution-precipitation reactions, with implications for predicting the fate of $CO_2$ in subsurface formations or alkaline waste piles (e.g., mine tailings).

## 2. Methods

### *2.1. Experimental Setup*

Two types of column experiments were used to investigate the effects of brucite grain size and water content on the carbonation reaction. The first consisted of three columns at 35% water saturation, with saturation defined as the ratio of water volume to pore volume. Each column contained a different size fraction of brucite, a 'very fine' fraction of <53 μm, a 'fine' fraction with particles between 53 and 180 μm, and a 'medium' fraction with particles ranging from 250 to 500 μm in diameter. The second set

of experiments consisted of columns with different water saturations: 15%, 35%, and 50%, all of which contained 'medium' brucite. These saturation values correspond to the total bulk water saturations, while the actual saturations varied somewhat with depth due to differences in elevation and capillary forces. Duplicate 15%, 35% and 50% saturated medium brucite columns were set up to assess the reproducibility of carbonation rates, but no solids were sampled from these duplicate columns. In order to assess the effect of fine particulates, which were produced during the crushing process and coated brucite surfaces, a triplicate 35% saturated medium brucite column was conducted using brucite that had been repeatedly rinsed with deionized water to remove these fine particles. All experiments were conducted in 16.0 cm × 5.9 cm polycarbonate columns manufactured by W.A. Hammond Drierite. These were filled with 10 wt.% pulverized brucite ore and 90 wt.% quartz sand to a height of 12.3-13.7 cm (Fig. 1). This brucite abundance is within the range of that typically observed in ultramafic mine tailings, which are of interest as a feedstock for $CO_2$ sequestration (e.g., Pronost et al. 2011; Assima et al., 2013b; Wilson et al., 2014). The brucite/quartz mixtures were prepared by mechanically mixing 45 g of brucite ore, and 405 g of quartz sand (total mass = 450 g). Solids were poured into columns and mechanically re-homogenized. The columns were tapped gently to allow solids to settle according to their intrinsic bulk density. The brucite ore was obtained from Premier Magnesia LLC, and was pulverized using a hammermill and sieved to separate into the appropriate size fractions. The quartz sand was a product of Lane Mountain Materials that had been sieved to <600 μm (median • 210 μm). The initial major oxide composition of the starting materials was determined using X-ray fluorescence spectroscopy (XRF; refer to Supplementary Material (SM) for details). XRF measurements of 5 duplicate samples indicated that the oxides present in the brucite ore

at • 1.00% ± 1 abundance were: MgO (60.16 ± 0.43%), $SiO_2$ (2.71 ± 0.04%), and CaO (2.04 ± 0.03%), with 34.29 ± 0.43% loss on ignition. Rietveld refinement of X-ray diffraction (XRD) data collected from analysis of triplicate samples of the medium brucite ore indicated it contained 78.8 ± 3.8 wt.% brucite, 5.5 ± 0.4 wt.% dolomite, 1.9 ± 0.3 wt.% magnesite, 7.4 ± 1.0 wt.% hydromagnesite, and <0.5 wt.% lizardite and pyroaurite. The remainder was amorphous content. Analysis of single samples of the very fine and fine size fractions indicated that there was no significant difference in mineral abundance between the different size fractions, except for magnesite which was equal to 2.7 wt.% and 4.0 wt.% in the very fine and fine size fractions, respectively. Analysis of duplicate quartz sand samples with XRF indicated that it was 97.94 ± 1.26% $SiO_2$ and • 2.49% $Al_2O_3$, and Rietveld refinement of XRD data indicated that it was nearly 100% pure with trace muscovite (• 0.9 wt.%). The surface area of the brucite ore was determined on duplicate samples using BET with $N_2$ adsorption, and was equal to 5.2 ± 0.2, 3.7 ± 0.3, and 2.4 ± 0.7 $m^2 g^{-1}$ for the very fine, fine, and medium brucite, respectively. The particle size distribution of the very fine and fine brucite was determined using a Malvern Mastersizer 2000 Laser Diffraction Particle Size Analyzer (SM Fig. S1). This indicated that the mean particle radius was 12 μm and 39 μm for the very fine and fine brucite, respectively. The medium brucite size fraction had a mean particle radius of 188 μm as estimated based on sieving results (SM Fig. S1). The porosity of the sediment in each column was calculated based on the density of the solids and the bulk volume of the porous media; it ranged from 0.49–0.53 (Table 1).

Initial solutions were prepared by dissolving $MgCl_2 \cdot 6H_2O$ from Fisher Scientific in deionized water to achieve a concentration of 0.1 M $MgCl_2$. This solution composition was used to facilitate comparison with previous brucite carbonation experiments that

utilized batch reactors (Harrison et al., 2013). The initial solutions contained $<4.0 \times 10^{-4}$ M dissolved inorganic carbon (DIC). The solution was slowly applied across the sediment surface in the columns and allowed to infiltrate the column under the force of gravity. The volume of solution added was dependent on the desired water saturation for each experiment (Table 1). Wetting fronts were observed to spread evenly across the diameter of the columns. Once they were observed to reach the base of the columns, the gas supply was initiated.

Columns were supplied with 10.0 vol.% gaseous $CO_2$ (90.0 vol.% $N_2$), through a hose barb at their base (Fig. 1). The gas streams were not humidified, and therefore induced evaporation from the columns. Gas was introduced to the base of the sediment through a stainless steel grate covered with fabric mesh. A Cole-Parmer Masterflex® L/S precision® standard pump system fitted with an L/S Easy-Load II® pump head was used to supply the gas stream at ~15 mL $min^{-1}$ (~$2.7 \times 10^{-3}$ g $CO_2$ $min^{-1}$) to each column at atmospheric pressure and room temperature (~21°C). The gas stream exited through a port at the top of each column to maintain close to atmospheric pressure within the column (Fig. 1). The $CO_2$ concentration of the gas effluent from each column was recorded at five minute intervals using Vaisala® GMT221 $CO_2$ concentration sensors. The accuracy of the sensor measurements varied between ± 0.5% to ± 2.0% depending on the measurement apparatus, which at times became contaminated with ambient laboratory air that diluted the effluent. Gas composition data were unavailable for the 15% saturated columns due to atmospheric contamination of the measurement apparatus. The $CO_2$ breakthrough is expressed as '$C/C_0$,' the ratio of the $CO_2$ concentration in the gas effluent at a given time to the measured $CO_2$ concentration of the gas effluent after the reaction was complete.

Experiments were conducted for time periods ranging from 160 to 261 h depending on the time required for the reaction to cease. Following completion of the experiments, solids were sampled by removing the entirety of the material in 2 cm intervals. The water saturation profile was estimated gravimetrically using the mass difference before and after samples were dried at room temperature. Solid samples were then analyzed for total inorganic carbon content using coulometry and mineral abundance using Rietveld refinement of XRD data (refer to SM). The solid samples were also prepared for characterization using scanning electron microscopy (SEM) both as disaggregated powders and as polished epoxy-embedded mounts to allow cross-sectional views of reacted grains. Experimental conditions including grain size, water content, and porosity are summarized in Table 1. For further detail regarding the experimental setup and analytical techniques, refer to the Supplementary Material.

*2.2. Assessment of reaction progress*

The mass of $CO_2$ sequestered was estimated using several lines of evidence, including (1) the total inorganic carbon content in the solid phase, (2) the mass gain of the columns during the course of the experiment, and (3) abundance of mineral phases. The total inorganic carbon content in all solid samples was determined using a CM5130 acidification module with a Model 5014 $CO_2$ Coulometer from UIC Inc. Samples were acidified to release $CO_{2(g)}$, which was quantified using a photodetector that monitors the colour change of a colourimetric pH indicator. The measured carbon content for all experiments is expressed as $\%CO_2$ by mass (wt.%). The initial brucite/quartz mixtures had an average of 0.67 ± 0.07% $CO_2$ based on analysis of 6 samples that was contained in dolomite, hydromagnesite, and magnesite present in the initial brucite ore. This initial

mass of $CO_2$ was subtracted from $CO_2$ content values measured for reacted samples to determine the mass of $CO_2$ gained. This was justified by the presence of approximately the same mass of dolomite in the reaction products as in the initial material, although the data were insufficient to resolve changes in hydromagnesite and magnesite abundances. To estimate the $CO_2$ gain gravimetrically, columns were placed on a scale with ± 0.01 g accuracy and their mass was recorded four times a day. At least one column in every experimental trial began to lose mass before the end of the experiment due to evaporation driven by the flux of dry $CO_2/N_2$ gas. Under the assumption that the evaporation rate remained relatively constant, this mass loss rate was applied to all experiments of a given trial to correct the gravimetric $CO_2$ measurements for evaporative loss over the entire duration of each experiment (i.e., measured mass gain + total evaporative loss = total $CO_2$ gain). An evaporation rate of ~0.01 g $H_2O$ $h^{-1}$ was estimated for all experiments, as is consistent with the expected vapour pressure of water in $N_2$ at the experimental conditions (~3 mol% $H_2O$; after Rigby and Prausnitz, 1967). Both total carbon and gravimetric measurements provided comparable estimates of the mass of $CO_2$ sequestered. The error on total carbon measurements was ± 0.22 g and was ± 0.04 g for gravimetric measurements. The error on gravimetric measurements is small compared to the uncertainty in evaporation rate calculations. However, the accuracy of reaction progress measurement is confirmed by good agreement between these two independent analyses.

The mass of $CO_2$ contained in crystalline carbonate phases was quantified using Rietveld refinement of XRD data. In order to determine whether $CO_2$ was also stored in non-crystalline phases, a known mass of a highly crystalline phase ([$CaF_2$] or [$Al_2O_3$]) was added to experimental samples. This allowed for quantification of poorly- or nano-

crystalline phases (e.g., Gualtieri, 2000). For further detail regarding extent of carbonation measurement methods and results, refer to the Supplementary Material.

Instantaneous carbonation rates ($r_{instant}$ in g $CO_2$ $h^{-1}$) were determined based on the mass gain between each measurement as follows (Eq. 1):

$$r_{instant} = \frac{[m_2 - m_1]}{[t_2 - t_1]} \qquad (1)$$

where $m_i$ is the column mass (g) at a given measurement time, and $t_i$ is the time of measurement (h).

*2.3. Reactive transport modelling*

The experimental conditions were modeled using the multicomponent reactive transport code MIN3P-DUSTY (Molins and Mayer, 2007) to elucidate reaction mechanisms and allow for calibration of a model to capture reaction progress during carbonation of brucite. MIN3P-DUSTY comprises a suite of chemical reactions including mineral dissolution-precipitation, and can model flow and transport in both the gas and aqueous phases. Gas transport was modeled as an advective-diffusive process according to Darcy's law and the Dusty Gas model (Mason and Malinauskas, 1983; Molins and Mayer, 2007). For a complete description of the constitutive equations refer to Mayer et al. (2002) and Molins and Mayer (2007). $CO_2$/$N_2$ gas supply rates were equal to those in the experiment. Brucite dissolution kinetics were modeled using a far-from-equilibrium $HCO_3^-$ concentration-dependent kinetic dissolution rate law based on data from Pokrovsky et al. (2005) and Pokrovsky and Schott (2004) (Eqs. 2 and 3):

$$r_{brc} = k^o_{eff}[HCO_3^-]^{0.56}(1 - \Omega^2) \qquad (2)$$

$$k^o_{eff} = k^0 SA \qquad (3)$$

where $k^{o}_{eff}$ is the effective rate constant, $k^{0}$ is the initial reaction rate constant equal to $10^{-6.13}$ L $s^{-1}$ $m^{-2}$, *SA* is the brucite surface area ($m^2$), and Ω is the saturation ratio. Saturation ratio is defined as the ratio of the ion activity product to the equilibrium constant. Modelling suggested that the pore water remained far-from-equilibrium with respect to brucite during carbonation. Although precipitation of both a poorly crystalline hydrated Mg-carbonate and nesquehonite [$MgCO_3 \cdot 3H_2O$] was documented in the experiments, thermodynamic data were unavailable for the poorly crystalline phase; therefore nesquehonite precipitation was used as a surrogate to represent precipitation of all secondary carbonate phases. Nesquehonite precipitation was effectively simulated as an equilibrium process, as is consistent with findings of Harrison et al. (2013). Porosity was set to a representative value of 0.53 for all simulations, and soil hydraulic function parameters were estimated based on results of Tempe cell tests of the solid materials (e.g., Fredlund and Rahardjo, 1993) and measured water saturation profiles. Porosity was updated as a function of the changing mineral volume fractions during reaction, and changes in permeability were approximated according to the Carman-Kozeny relationship (e.g., Bear, 1972). Although this is an approximation only, modelling outputs were found to be most sensitive to changes in brucite reactivity as opposed to physical input parameters. $CO_2$ breakthrough curves measured in the experiments were used as a fitting parameter to estimate effective reactive surface areas and interpret reaction mechanisms. For a complete list of transport parameters used in the simulations, refer to the Supplementary Material.

## 3. Results

### *3.1. Instantaneous carbonation rates and $CO_2$ breakthrough*

The replacement of brucite by carbonate phases was evident in all experiments (Figs. 2-3). Four distinct stages in the carbonation reaction were identified, with each stage typified by a distinct trend in carbonation rate and $CO_2$ breakthrough (Figs. 4-5). Although all stages were reproducible in duplicate experiments, the presence of each stage was dependent on the experimental parameters (Figs. 4 and 5). Specifically, stage 1 was absent from the very fine and fine brucite column experiments, and stage 2 was absent from the 15% saturated medium brucite columns.

Stage 1 in the medium brucite columns was demarcated by rapid carbonation rates (up to ~0.16 g $CO_2$ $h^{-1}$) for the first ~1-2 h of the experiment, which corresponded to periods of negligible $CO_2$ in the outflow (Figs. 4c and 5c-d). Because conservative flushing of one pore volume in the columns would take approximately 0.1 h in these columns, the period with negligible $CO_2$ in the outflow is attributed to it being trapped in the column, in both the solid and aqueous phase.

Stage 2 was typified by periods of relatively constant reaction rates, and consequently, relatively constant $CO_2$ concentrations in the gas effluent (Figs. 4b-c and 5). In both the very fine and fine brucite columns, stage 2 persisted for the first ~68 h, during which little to no $CO_2$ was measured at the column outlet (Figs. 4b and 5a-b). Carbonation rates during this period were on average 0.15 g $CO_2$ $h^{-1}$ in both columns (Table 2). Similarly, in the 35% and 50% saturated medium brucite columns, stage 2 was marked by relatively constant carbonation rates, and relatively constant, but elevated $CO_2$ concentrations in the gas effluent of 4.0-5.0% and 5.0-6.0% $CO_2$, respectively (Figs. 5c-d). Rates were between 0.08 and 0.11 g $CO_2$ $h^{-1}$ in the 35% saturated columns, and between 0.07 and 0.10 g $CO_2$ $h^{-1}$ in the 50% saturated columns. Carbonation rates in the

finer grained brucite columns exceeded those in the medium brucite columns on average by 1.6-1.9 times during stage 2.

In stage 3, carbonation rates declined steadily in all experiments, with a concurrent increase in the $CO_2$ content of the gas effluent (Figs. 4b-c and 5). During stage 3, the $CO_2$ content increased to ~7.5% and 8.0% $CO_2$ in the very fine and fine brucite columns, respectively, and to ~9.5-10.0% in the 35% and 50% saturated medium brucite columns (Fig. 5). Transient sharp changes in $CO_2$ content over short durations (i.e. ~1 h) are attributed to disturbance of the $CO_2$ content measurement vials during column mass measurements (Fig. 5). Although gas composition data were unavailable, stage 3 was evident in the 15% saturated medium brucite column, with carbonation rates declining throughout the experiment and becoming negligible after ~97 h (Fig. 4c).

Stage 4 was evident in all columns, and was defined by a period of negligible carbonation rate and relatively constant $CO_2$ concentration in the gas effluent, approximately equal to the composition of the supplied gas within the estimated measurement error (Figs. 4b-c and 5). Although the final $CO_2$ content of the gas effluent did not exactly equal the inlet composition in the very fine and fine brucite columns, the lack of mass gain after ~115 hours (Fig. 4a), and the near complete depletion of brucite in these experiments (Fig. 2) clearly indicate that stage 4 is coincident with the effective cessation of the carbonation reaction.

### *3.2. Reaction progress*

The total mass of $CO_2$ sequestered as determined using carbon content (%$CO_2$) measurements indicated that a total of 16.8 g, 13.1 g, and 9.0 g $CO_2$ were sequestered in the very fine, fine, and medium brucite columns at 35% saturation, respectively (Table 2).

A total of 5.2 g, 9.0 g, and 8.6 g $CO_2$ were sequestered in the 15%, 35%, and 50% saturated medium brucite columns, respectively (Table 2). Similarly, 9.3 g $CO_2$ were sequestered in the 35% saturated column with rinsed medium brucite (Table 2). The $\%CO_2$ measurements with depth are provided in the Supplementary Material (Tables S8 and S9). These values are in very good agreement with those determined gravimetrically (Fig. 4a; Table 2).

In all experiments, brucite was replaced by a combination of the hydrated Mg-carbonate mineral, nesquehonite, and an amorphous or nano-crystalline solid phase that could not be resolved using XRD (SM Fig. S2). There was no evidence that silicate phases were formed. The abundance of the X-ray amorphous phase as determined using Rietveld refinement included any non-crystalline content in the initial materials. However, it is the relative trends in amorphous content that are important, rather than the absolute values. The total mass of $CO_2$ sequestered in each column was significantly greater than can be attributed to the measured abundance of nesquehonite (Table 2). Although the dissolved inorganic carbon concentration of the pore water was not directly measured, measurements from similar experimental systems suggest it is unlikely to exceed ~0.18 M (Harrison et al., 2013). This would correspond to a maximum of ~0.8 g $CO_2$ in the aqueous phase, and thus cannot account for the mass discrepancy, which was as high as 12.8 g $CO_2$ (Table 2). This implies that the unidentified phase quantified using the XRD data is a carbonate phase, as confirmed with energy dispersive spectroscopy (Fig. 6c).

The greatest extent of carbonation in terms of the mass of brucite converted to carbonate was achieved in the very fine brucite column at 94%, followed by the fine brucite column at 81%. A similar extent of carbonation was documented in the 35% and

50% saturated medium brucite columns, at 59% and 58%, respectively. The lowest extent of carbonation was attained in the 15% saturated medium brucite column at 35%.

The abundance and distribution of nesquehonite, the poorly crystalline carbonate phase, and total $CO_2$ sequestered varied significantly between experiments of different grain size (Fig. 2). Both the very fine and fine brucite columns exhibited similar $\%CO_2$ trends, with the greatest $CO_2$ content near the column inlet (Fig. 2). Similarly, brucite abundance was lowest at the column inlet, where nesquehonite abundance tended to be highest (Fig. 2). Although a similar extent of carbonation was achieved in the 35% and 50% saturated columns, the distribution of brucite and carbonate precipitates differed (Fig. 3). In the 35% saturated column, total $CO_2$ content and nesquehonite abundance decreased along the flow-path, whereas nesquehonite, brucite, and total $CO_2$ were more evenly distributed throughout the 50% saturated column (Fig. 3). The poorly crystalline carbonate phase increased in abundance along the flow-path in all 35% saturated columns, but was more abundant with depth in the 50% saturated medium brucite column (Figs. 2 and 3). The total $CO_2$ content in the 15% saturated medium brucite column was effectively constant along the flow-path (Fig. 3a).

*3.3. Qualitative characterization of solids*

SEM micrographs of the initial material revealed that the brucite grains were coated by brucite powder, an artifact of the crushing process (Fig. 6a). Reaction products were comprised of elongated, narrow crystals, consistent with the morphology of nesquehonite (Ferrini et al., 2009; Harrison et al., 2013a), and flakey material similar to that documented for other hydrated Mg-carbonate-hydroxide phases, such as dypingite (e.g., Power et al., 2007; Power et al., 2009; Power et al., 2013b; Figs. 6b-c). Energy

dispersive spectroscopy confirmed that both crystal morphologies consisted of Mg, C, and O (Fig. 6c; SM Fig S4). The observed abundance of flakey material was greater in the very fine and fine brucite columns than in the medium brucite columns, and generally increased along the flow path. We interpret the flakey material to represent the poorly crystalline carbonate-hydroxide phase, as the observed trend in abundance of this material along the flow path in the very fine and fine columns is consistent with the XRD data (Figs. 2a-b). The nanometre scale thickness of the carbonate flakes is consistent with its X-ray amorphous nature, as the crystals may be too small to exhibit long-range order that can be resolved using XRD. Cross-sectional views of reacted grains from the medium brucite columns showed that carbonate precipitates generally surrounded and coated unreacted brucite, whereas quartz surfaces typically remained uncoated (Fig. 6b). In some instances brucite grains had one or more sides lacking carbonate precipitates (Fig. 6b). Conversely, in the very fine brucite columns, carbonate precipitates formed interstitial cement that filled pore spaces between brucite and quartz grains (Fig. 6d). Nesquehonite rinds appeared non-porous at a submicron scale (Figs. 6e-f).

*3.4. Water content*

Final water content measurements are provided in terms of the ratio of water volume to bulk porous media volume (volumetric water content) rather than water saturation, owing to possible changes in pore volume due to carbonation. In the 35% saturated columns, a water loss of 28% (16.2 g), 28% (16.3 g), and 22% (15.9 g) was measured in the very fine, fine, and medium brucite columns, respectively. In the 15%, 35%, and 50% saturated medium brucite columns, a water loss of 37% (10.6 g), 22% (15.9 g), and 17% (16.5 g) was recorded, respectively. Initial water volumes are provided

in Table 1. Water loss occurred via evaporation and incorporation into precipitates. The very fine and fine brucite columns had final volumetric water contents (VWC) ranging between 0.09-0.17, compared to an initial bulk VWC of 0.17 (35% saturation) (SM Fig. S3). VWC increased with depth and ranged from 0.08-0.24 and 0.17-0.30 in the 35% and 50% saturated medium brucite columns, respectively (SM Fig. S3). In the 15% saturated medium brucite column the VWC remained relatively constant with depth, at values between 0.04 and 0.06 compared to an initial bulk VWC of 0.08 (SM Fig. S3). Water movement during reaction likely led to its redistribution as the reaction progressed.

The mass of water lost in all experiments is much greater than can be attributed to evaporation alone. An approximate evaporation rate of 0.01 g $H_2O$ $h^{-1}$ was estimated for all experiments throughout their duration (refer to Methods), equating to between 1.8 and 3.3 g water lost from all experiments. Between 69% and 89% of water lost from the pore space in the columns is therefore attributed to incorporation into hydrated carbonate phases. The mass of water in nesquehonite is insufficient to account for the total water mass incorporated into the solid phase. Based on the ideal stoichiometry of nesquehonite (3 moles water per mole nesquehonite) it contained only ~8-35% of the water attributed to the solid phase. This implies that the poorly crystalline carbonate was also a hydrated phase, as is expected under the experimental conditions (Hänchen et al., 2008).

*3.5. Reaction stoichiometry*

In order to model the carbonation reaction, it is important to quantify the reaction stoichiometry to accurately represent the mass of $CO_2$ that can be sequestered for a given mass of brucite reacted. The reaction stoichiometry for conversion of brucite to nesquehonite is 1 mole brucite per mole $CO_2$. However, the presence of the poorly

crystalline hydrated carbonate phase complicates the overall reaction stoichiometry for the brucite carbonation reaction. Mass balance calculations based on XRD and $\%CO_2$ data reveal that if the unidentified carbonate is a single phase, the Mg:$CO_2$ ratio in this phase is ~2. In order to maintain charge balance, this implies that the unidentified phase is likely a hydroxy-carbonate with a formula of $Mg_2CO_3(OH)_2 \cdot xH_2O$, similar to that of the Mg-carbonate, artinite [$Mg_2CO_3(OH)_2 \cdot 3H_2O$]. Based on the water mass balance in each experiment, it is estimated that 'x' is between 1 and 3 (average 2).

No thermodynamic data were available to directly model precipitation of the poorly crystalline carbonate phase. Thus, the reactive transport models were simplified such that nesquehonite precipitation represented formation of all carbonate precipitates. This maintains the experimental $CO_2$, $OH^-$, and Mg balance. Because the formation of the poorly crystalline carbonate reduced the ratio of $CO_2$ stored per mole of Mg, the initial brucite content in the models was treated as a fitting parameter to match the measured overall reaction stoichiometry. This was done rather than changing the stoichiometry of nesquehonite to avoid alteration of its solubility product and equilibrium constant.

The overall reaction stoichiometry was also calculated using the experimental data. The reduction in brucite mass and the total $CO_2$ mass gain in each column were determined with XRD and solid phase $CO_2$ measurements, respectively. The stoichiometric ratio was then calculated according to the following equation (Eq. 4):

$$\frac{Mg}{C} = \frac{\left[n_{brc_i} - n_{brc_f}\right]}{\left[n_{CO_{2_f}} - n_{CO_{2_i}}\right]} \qquad (4)$$

where $\frac{Mg}{C}$ is the ratio of moles Mg consumed to moles $CO_2$ sequestered, $n_{brc_i}$ is number of moles of brucite initially in the column, which was determined to be 0.61 ± 0.02 moles (1 ), $n_{brc_f}$ is the moles of brucite at the end of the experiment, and $n_{CO_{2_i}}$ and $n_{CO_{2_f}}$ are

the moles of $CO_2$ in the solid phase at the beginning and end of the experiment, respectively. The values of $\frac{Mg}{C}$ for the 35% saturated very fine, fine, and medium brucite columns were 1.5, 1.7, and 1.8, respectively, compared to 1.0 for conversion to pure nesquehonite. The medium brucite columns at 15%, 35%, and 50% saturation all had $\frac{Mg}{C}$ values of 1.8, and the average $\frac{Mg}{C}$ from all experiments was 1.7. Due to the inherent measurement error in the brucite and $CO_2$ contents, and the variation of brucite content in the initial brucite ore, these values were not directly input in the models. However, the model-fitted values were in good agreement with the calculated values, and are provided in the SM. The reaction stoichiometry, along with reaction rates and extent of carbonation are summarized in Table 2.

## 4. Discussion

### *4.1. Reaction stages*

Both the absolute carbonation rate and the reaction stages were strongly influenced by brucite grain size, but were relatively insensitive to water content when above 15% initial saturation (Fig. 4). In general, higher reaction rates were achieved with finer grain size due to the greater specific surface area of the finer particles (Tables 1 and 2). Another key difference between the grain sizes was the absence of stage 1 in the very fine and fine brucite columns. Stage 1 is distinguished from the similarly high stage 2 reaction rates in the very fine and fine brucite columns due to its comparatively short duration (Figs. 4b-c). This transient rapid reaction rate is attributed to the carbonation of the brucite powder that was observed at the surface of larger brucite grains (Fig. 6a). It is expected that these finer particles reacted rapidly and were consumed in the first ~1-2

hours of the experiment owing to their higher surface area (Fig. 7; Helgeson et al., 1984; Andreani et al., 2009; Assima et al., 2013a). Although stage 1 may occur in the very fine and fine brucite columns, it remains unresolved due to the similarly high reaction rate of the bulk material.

Stage 2 is demarcated by a period of relatively constant carbonation rates in all experiments, and near constant $CO_2$ concentration in the effluent gas (Figs. 4 and 5). This represents carbonation of the bulk of the brucite (Fig. 7). The non-zero (~4-6%) outlet $CO_2$ concentration during stage 2 is unique to the medium brucite columns (Fig. 5). Slight declines in $CO_2$ concentration during this period may be due to an increase in carbonate precipitation rate after initial nucleation has occurred.

In all experiments, the final decline in reaction rate and increase in outlet $CO_2$ concentration during stage 3 (Figs. 4 and 5) is attributed to a decrease in the abundance of reactive brucite along the column length. Finally, stage 4 is reached when the reaction rate has declined sufficiently such that $CO_2$ flow through the column is effectively conserved (Fig. 7).

*4.2. Controls on reaction*

Over this range of experimental conditions, several controls on reaction were realized, including: $CO_2$ supply, brucite dissolution, and water content. During stage 2 in the very fine brucite column, negligible $CO_2$ was vented (Fig. 5a), and the rate of $CO_2$ supply to the column was approximately balanced by the rate of brucite carbonation (Fig. 8). This implies that the overall carbonation rate was limited by the rate of $CO_2$ supply to the column (Fig. 8); an increase in the $CO_2$ flux would therefore accelerate carbonation. Conversely, in the medium brucite columns, only ~40-60% of the supplied $CO_2$ is

captured before reaching the column outlet, indicating that the rate of $CO_2$ supply outpaced the rate of carbonation. Thus, the carbonation rate of medium brucite was limited either by the rate of brucite dissolution, carbonate precipitation (Fig. 8), or lack of available water (e.g., Schaef et al., 2011; Assima et al., 2013a). Under similar experimental conditions, it has been documented that carbonate precipitation occurs relatively rapidly, and is therefore unlikely to be rate limiting (Wilson et al., 2010; Harrison et al., 2013a).

The fine brucite experiment represents the transition between these two "endmembers" of rate limitation. The low but measureable amount of $CO_2$ vented during stage 2 (Fig. 5b), and the slightly lower rate of reaction compared to the very fine brucite (Fig. 4b) suggests that the rate of $CO_2$ supply slightly exceeded the carbonation rate. Thus, the moderate decrease in reactive surface area between the very fine and fine brucite sufficiently lowered the rate of brucite dissolution to shift the overall reaction from being $CO_2$ supply to mineral dissolution limited (Fig. 8). However, in both the fine and medium brucite columns, a significant portion of brucite was not carbonated despite the effective cessation of the reaction before the end of the experiment (Fig. 4c). This implies that brucite carbonation became inhibited at some point during the reaction.

The extent of carbonation was strongly dependent on the initial grain size; the amount of brucite consumed in the 35% water saturated columns declined from 94% to 82% to 63% in very fine, fine, and medium brucite columns, respectively (Table 2). As is consistent with results of Assima et al. (2013a) for carbonation of chrysotile mining residues, reaction progress was restricted at low water content. Only 41% of the brucite was reacted in the column with the lowest water saturation (15% saturated). It is possible

that the incomplete reaction of brucite within the timeframe of the experiments can be attributed to a reduction in total brucite surface area as it is consumed, leading to a decline in the bulk brucite dissolution rate. In reactive transport models, the decrease in total surface area with dissolution is commonly updated assuming particles can be represented by a uniform population of perfect spheres or cubes that shrink as they dissolve (e.g., Lichtner, 1996; Mayer et al., 2002; Appelo and Postma, 2005; Wanner et al., 2011). This is described by the following equation, henceforth designated the 'geometric model' (Eq. 5; Mayer et al., 2002):

$$k_{eff}^{g} = (k^{0} SA)\left(\frac{\varphi^{t}}{\varphi^{0}}\right)^{2/3} \quad (5)$$

where $\varphi^0$ is the initial mineral volume fraction, and $k_{eff}^{g}$ and $\varphi^t$ are the effective geometric reaction rate constant and mineral volume fraction at a given time greater than zero, respectively. Here, $k_{eff}^{g}$ replaces $k_{eff}^{0}$ in Equation 2. This function calculates the decline in reactive surface area that is geometrically related to the consumption of the initial material (i.e., when $\varphi^t$ shrinks), where the '2/3' exponent represents the ratio of the surface area of a sphere to its volume. This function was applied in MIN3P-DUSTY to model the experimental conditions and was compared against experimental data. Owing to the similarity in the $CO_2$ breakthrough curves of the 50% and 35% saturated columns, and the lack of data for the 15% saturated column, the 35% saturated columns were the only medium brucite columns that were modeled. The presence of the powder coating the bulk brucite (Fig. 6a) was included in the model by incorporating a small mass of brucite with a significantly higher surface area than the bulk material (stage 1). The removal of this surface powder corresponds to the sharp increase in $CO_2$ concentration in the gas effluent after ~2 h of reaction (Figs. 5c-d). The very similar

extent of carbonation achieved in the rinsed medium brucite column confirms that reaction of the powder comprised only a small fraction of the total brucite consumed (Fig. 3b).

Application of the geometric model to simulate the very fine brucite column reproduced the $CO_2$ breakthrough curve and extent of reaction in the very fine brucite column very well with an adjustment of the initial reactive surface to ~20% of the BET measured surface area (Fig. 5a). The BET surface area is often an overestimate of the true reactive surface area, due to variability in the reactivity of surface features and the inclusion of "internal" surface area in BET measurements, which may be less reactive than the actual "external" surface area (Brantley and Mellot, 2000; Gautier et al., 2001; Luttge and Arvidson, 2008). The reduction of the initial brucite surface area in the model is justified to account for these effects. The same reduction in reactive surface area was thus employed to model the fine and medium brucite columns.

The geometric model predicts a gradual decrease in reaction rate during stage 2 due to consumption of the bulk material and the reduction in total surface area. Yet, it cannot reproduce the precipitous shut down of reaction prior to complete consumption of the brucite in the fine and medium brucite columns, as evidenced by the poor fit between the modeled and experimental data ('geometric model' in Fig. 5). There are several hypotheses that could explain this incomplete reaction and precipitous decline in reaction rate: 1) water-limited reaction, 2) a disproportionate decline in reactive surface area over time due to preferential consumption of highly reactive surface sites and finer grains during the early stages of the reaction, and 3) a loss of effective reactive surface area due to passivation of the brucite surface via carbonate precipitation. The two latter hypotheses

are mechanisms by which brucite dissolution may be limiting, whereas water-limited reaction affects both brucite dissolution and carbonate precipitation. We evaluate these hypotheses in light of the available data to discern the primary cause for the lack of reactivity in each column, and to allow reaction progress to be better modeled.

*4.2.1. Water-limited reaction*

Water is required not only as a reaction medium to solubilize and transport ions, but also as a reactant to form hydrated Mg-carbonate phases that incorporate water in their crystal structures. The distribution of water may therefore be a strong control on the extent of carbonation at the grain scale. At low water contents, water is held primarily around grains and in pore throats as opposed to larger pore spaces. Thus, the wetted pore volume available for precipitation is limited, and precipitation of carbonate phases may largely be restricted to the area immediately surrounding brucite grains (Fig. 6b). Although pH was not directly measured, previous experimental results suggest it would drop from ~9.3 to ~7.6 during brucite carbonation (Harrison et al., 2013). However, gradients in pH and solute concentrations at the pore scale may lead to variation in saturation state within pores. In the medium brucite columns for instance, the quartz grains were generally not coated with carbonate (Fig. 6b), suggesting that the interfacial fluid in contact with quartz may have been undersaturated with respect to carbonate phases. Alternatively, the carbonates may favour nucleation on brucite grains compared to quartz. For example, Stockmann et al. (2014) demonstrate that carbonate precipitates preferentially nucleate on certain mineral substrates over others, which is attributed in part to the degree of mismatch in crystal structure between the nucleating phase and the

substrate. In any case, without nucleation on quartz, the volume in which carbonate precipitates may form is further restricted.

The incorporation of water in the crystal structure of hydrated Mg-carbonate phases means that there is a stoichiometric limit to the mass of $CO_2$ that can be stored based on the amount of water available. For example, Schaef et al. (2011) demonstrate that the volume of water available to incorporate into nesquehonite dictates the extent of brucite carbonation in wet supercritical $CO_2$. If all the brucite in the columns were converted to nesquehonite, two moles of water would be required per mole of brucite consumed (Eq. 6). Thus, 22 g (1.22 moles) of water are required to convert the initial 0.61 moles of brucite to nesquehonite. The initial volume of water added to the columns exceeded this limit for all experiments (Table 1). Moreover, in all but the 15% saturated medium brucite column, even the final water saturation is in excess of this value for the entire depth of the column (SM Fig. S3).

$$Mg(OH)_2 + CO_2 + 2H_2O \rightleftharpoons MgCO_3 \cdot 3H_2O \qquad \text{Eq. (6)}$$

Thus, an insufficient supply of water can explain the lack of carbonation in the 15% saturated column, but cannot account for incomplete carbonation in the other columns. The distribution of water at the pore scale is likely heterogeneous and leaves some grains relatively dry, suggesting that the true reactive capacity may be lower than the theoretical stoichiometric limit. Still, the near complete consumption of brucite in the very fine brucite column with the same water content as the fine and medium brucite 35% saturated columns confirms that the lower extent of reaction cannot be attributed to insufficient water. The similar extent of reaction achieved in both the 35% and 50%

saturated medium brucite columns, despite the difference in water volume is consistent with this conclusion.

*4.2.2. Consumption of highly reactive sites and fine grains*

An alternative hypothesis to explain the incomplete reaction in these columns is that the net surface area of the brucite is progressively reduced due to the preferential consumption of the finest grains in each size fraction during the early stages of the reaction. Neglecting the powder coating, the geometric specific surface area of the finest particles within the medium brucite size fraction is within a factor of three of the coarsest grains, assuming spherical particles. This difference is too small to explain the effective shutdown of the reaction. It is also possible that the pulverization of the initial brucite induced defects at the mineral surface with higher reactivity than the underlying material (White and Brantley, 2003). As these highly reactive sites are consumed, the reaction rate would decline. For example, Petrovich (1981) shows that dissolution rates of ground quartz are higher during removal of a ~3 nm surface layer altered by grinding. However, at least 60% of the brucite is consumed prior to the stage 3 rate decline for brucite of all grain sizes; it is unlikely that reaction at these grinding induced reactive sites alone could consume such a large proportion of the brucite. Moreover, the >80% consumption of brucite in the very fine and fine columns implies that a significant proportion of coarser grained material in each size fraction is reacting along with the fines. Thus the preferential consumption of highly reactive sites and finer grains cannot explain the rapid shut off of the reaction prior to completion.

*4.2.3. Surface passivation*

The surface passivation hypothesis is most consistent with the experimental data, for all but the 15% saturated, water-limited columns. Scanning electron micrographs clearly depict carbonate precipitates forming a rind (10s-100s of microns) surrounding an unreacted brucite core, and as pervasive coatings on mineral surfaces (Fig. 6B-F). However, the presence of a surface coating does not necessarily imply that the surface is passivated. Reports in the literature on the effect of surface coatings are highly variable. For example, experimental studies using stirred or agitated reactors found that precipitation of calcite did not inhibit dissolution of basaltic glass or diopside (Stockmann et al., 2011; Stockmann et al., 2013), and amorphous Fe-rich, silica-free, coatings did not affect anorthite dissolution (Hodson, 2003). On the other hand, the rate of pyrite oxidation is slowed by precipitation of oxide coatings (Nicholson et al., 1990), and the reaction of Ca-rich steel making slags and cement kiln dust with $CO_2$ is inhibited by precipitation of calcium carbonate coatings (Lekakh et al., 2008; Huntzinger et al., 2009). Similarly, silica rich layers have been found to passivate the surfaces of olivine and serpentine, although the effect is lessened for basalt (Park and Fan, 2004; Béarat et al., 2006; Andreani et al., 2009; Daval et al., 2011; Sissmann et al., 2014; Johnson et al., 2014). However, the passivating effects of silica-rich layers are dynamic, and dependent on the presence of iron oxides or $Fe^{3+}$ in the silica layer (Saldi et al., 2013; Sissmann et al., 2013), and Pokrovsky and Schott (2000) show that the development of a silica-rich layer depends strongly on fluid chemistry. Daval et al. (2009a) and Hövelmann et al. (2012a) show that precipitation of calcium carbonate and magnesite can inhibit reaction

of wollastonite and olivine, respectively, while Montes-Hernandez et al. (2012) showed that $CaCO_3$ formation only passivated $Ca(OH)_2$ under isothermal conditions.

Despite the disagreement in the literature as to the effect of secondary phases on dissolution, the extent of passivation is typically a function of the degree of coverage of the primary phase surface and the density and permeability of the secondary phases (e.g., Cubillas et al., 2005; Daval et al., 2009a; Daval et al., 2009b). For example, Daval et al. (2009b) show that porous silica layers are not passivating for wollastonite carbonation until the porosity of this layer becomes clogged with calcite precipitates. The degree of passivation was also dependent on the microstructure of the secondary calcite (Daval et al., 2009a). At circum-neutral pH, the precipitation of many small calcite crystals formed denser, more impermeable layers and greater passivation than at acidic pH. Similarly, Cubillas et al. (2005) found that epitaxial growth of otavite [$CdCO_3$] coating a calcite surface inhibited dissolution, but its formation as islands rather than layers on aragonite [$CaCO_3$] surfaces did not slow dissolution. In the case of brucite, hydrated carbonates tend to favour upward growth of islands, but these islands may form a continuous layer over time (Hövelmann et al., 2012b), consistent with our observation of carbonate coatings. In our experiments, the degree to which these coatings are passivating may depend on which carbonate phase is dominant (i.e., the flakey poorly crystalline phase or crystalline nesquehonite). Velbel (1993) highlights the importance of the molar volume ratio of product to reactant for the extent of passivation, indicating that it must exceed 1 in order to completely passivate the surface. In any case, hydrated Mg-carbonates tend to have higher molar volume than brucite (e.g., brucite = 24 $cm^3$ $mol^{-1}$, nesquehonite = 75 $cm^3$ $mol^{-1}$), increasing the chances of passivation and pore clogging. SEM images of the

flakey Mg-carbonate phase indicate that although it can completely coat brucite grains, it has a relatively porous structure that may not significantly inhibit transport (Fig. 6c). Nesquehonite, on the other hand, forms thick rinds that exceed 100 μm in places, with a low porosity, bladed microstructure (Fig. 6b, e-f). This low porosity coating is likely to substantially inhibit reaction.

The geometric surface area update model does not account for these effects, resulting in the poor fit with the experimental data (Fig. 5). We instead develop an empirical function that successfully reproduces the instantaneous carbonation rate through time (as represented by the $CO_2$ breakthrough curves; Fig. 5). The proposed model relates the reactive surface area at a given time to the extent of conversion of brucite, allowing a relatively constant rate of reaction up to a threshold degree of conversion (SM Fig. S5). At this threshold, the reaction rapidly shuts down with increasing brucite consumption. This function is henceforth referred to as the 'threshold model' (Eq. 7):

$$k_{eff}^{t} = (k^{0}SA)\left[1 - \left(\frac{\varphi^{0} - \varphi^{t}}{\varphi^{0} - \varphi^{p}}\right)^{n}\right] \qquad (7)$$

the equation is valid for $\varphi^{t} \leq \varphi^{p}$, where $k_{eff}^{t}$ is the effective threshold rate constant and $\varphi^{p}$ is a threshold brucite volume fraction (i.e., conversion threshold) at which the reaction rate becomes negligible (stage 4). Here, $k_{eff}^{t}$ replaces $k_{eff}^{0}$ in Equation 2. The value of $\varphi^{p}$ was equal to the amount of brucite remaining in the lower half of each column, and the exponent $n$ was adjusted to provide the best fit with the experimental $CO_2$ breakthrough curves. A value of $n = 5$ provided the best fit to the experimental data for all grain sizes. The requirement of such a large exponent implies that the reaction shuts down rapidly when the conversion threshold is reached. The threshold model

produces excellent agreement with the experimental $CO_2$ breakthrough curves for all of the brucite grain sizes (Figs. 5a-c). A modest decrease in initial specific surface area equal to ~15% of the measured BET surface area for each grain size was employed.

Although the threshold model is empirically derived, its form provides valuable insight as to the mechanism of reaction. Similar behavior has been documented for diffusivity in weathering rinds on basalt clasts: upon reaching a threshold porosity, the pore space becomes interconnected, and diffusivity increases considerably (Navarre-Sitchler et al., 2011). During brucite carbonation, the threshold may represent a sudden decrease in porosity of both the bulk porous media and the carbonate surface coatings due to the transformation from the poorly crystalline flakey Mg-carbonate phase to crystalline nesquehonite. Although nesquehonite decreased in abundance along the flow path of the columns, the total $CO_2$ sequestered remained relatively constant (Figs. 2-3). This indicates that nesquehonite may have formed via replacement of a metastable carbonate phase, starting with the earliest-formed carbonate at the beginning of the flow path. Such a reaction path is not uncommon in the Mg-carbonate system (e.g., Hänchen et al., 2008; Schaef et al., 2011; Felmy et al., 2012; Schaef et al., 2013). Poorly crystalline phases are often precursors to more crystalline phases due to a lower mineral-solution interfacial energy (Steefel and Van Cappellen, 1990; Hellevang et al., 2013); the flakey Mg-carbonate may represent such a precursor. Thus, the shutdown of the reaction may relate to the conversion of the porous, poorly crystalline phase to low porosity nesquehonite. This is consistent with the lack of passivation in the very fine-grained column, as the rapid brucite dissolution rate may facilitate complete conversion to carbonate prior to the nesquehonite phase transformation. In the medium brucite columns, on the other hand,

the slower brucite dissolution rate may cause simultaneous brucite dissolution and carbonate transformation, inhibiting dissolution prior to complete consumption. If this were the case, the overall reaction rate in the latter stages of carbonation would depend on the kinetics of the transition between the flakey phase and nesquehonite. It has recently been noted that the kinetics of carbonate precipitation may be an important control on the overall carbonation reaction (Pham et al., 2011; Gautier et al., 2014), but the effect of Mg-carbonate phase transitions on surface passivation have not previously been considered to our knowledge. Because the rate of transition between the carbonate phases is unknown, we cannot directly model this effect, and thus rely on the empirical function. However, the empirical formulation is able to describe the evolution of reactivity at the macroscale as a function of reaction progress and surface passivation, consistent with mineralogical observations, and provided insight into reaction progress. Detailed studies of the brucite-carbonate interface are required to further evaluate the effect of the phase transformation on the porosity of the surface coating and to develop a mechanistic model of surface passivation. Similar to the model of Navarre-Sitchler et al. (2011), an alternative explanation for the rapid shutdown in reaction, is that at a threshold brucite conversion, a sufficient volume of carbonate has formed, such that the porosity in the surface coating becomes disconnected and effectively shuts off access to the brucite surface. In either case, the effective cessation of reaction prior to complete conversion of the brucite is attributed to surface passivation, although the exact mechanism of passivation cannot be directly assessed based on the current results.

## 5. Implications

*5.1. Reactive transport modelling*

Recent studies have highlighted the need for improved reactive transport models to predict the fate of $CO_2$ during subsurface geologic storage. In particular, better constraints on secondary phase nucleation and precipitation kinetics are necessary (Pham et al., 2011; Paukert et al., 2012; Hellevang et al., 2013; Galeczka et al., 2014; Gautier et al., 2014). Our experiments have highlighted the importance of phase transitions in the Mg-carbonate system for surface passivation and pore space clogging, a potentially important effect during subsurface injection of $CO_2$ into Mg-bearing rock, and formation of natural, serpentinite-hosted magnesite deposits (Boschi et al., 2009). These same mechanisms may inhibit carbon sequestration in alkaline industrial wastes. While a mechanistic model for passivation remains elusive, the excellent agreement between modeled and experimental results indicates that thresholding processes represent real constraints on carbon sequestration efficiency. The mechanism behind the passivating effects requires further study in order to develop a more generally applicable mechanistic model. Importantly, the reactive transport modelling demonstrated that conventional geometric models alone do not adequately reproduce reaction progress during brucite carbonation, hindering the ability to predict the fate of $CO_2$ injected in the subsurface or alkaline waste storage facilities. For example, similar $CO_2$ breakthrough curves have been documented during carbonation of coal fly ash in column reactors (Jo et al., 2012). This also has implications for modelling of reaction progress in natural systems that involve coupled dissolution-precipitation reactions, as the reactive surface area may not evolve in a straightforward manner. For example, the porosity and morphology changes associated with phase transformations may be relevant for other mineral systems. In particular, Mg-

sulfate, zeolite, and smectite minerals may undergo transitions between different hydration states at low temperatures, with relevance for bioavailability of water and nutrients in dry environments (e.g., Bish et al., 2003; Wilson and Bish, 2012). In unsaturated porous media, the effective reactive surface area may be reduced due to the decreased exposure to the reactive fluid (White and Brantley, 2003 and references therein). Experimental evidence indicates that inclusion of water-limited reaction in terms of its effect on the reactive capacity, rather than just the rate, may also be required for modelling reactions in unsaturated porous media involving hydrated mineral phases.

*5.2. $CO_2$ sequestration*

Surface passivation and water limitations are potentially important constraints for carbonation efficiency of mafic and ultramafic materials, although physical and chemical heterogeneities and more complex chemistry limit direct extrapolation from the experiments to field scale. Injection of supercritical $CO_2$ in the subsurface displaces formation water, resulting in a potentially water-limited reaction zone, and phase transitions between Mg-carbonates are common under these conditions (Loring et al., 2011; Schaef et al., 2011; Van Pham et al., 2012; Schaef et al., 2013; Miller et al., 2013). Phase transformations in the Mg-carbonate system may also have implications for formation of natural Mg-carbonate deposits. For example, Boschi et al. (2009) postulate that hydrous carbonate may have formed as a precursor to magnesite in serpentinite-hosted veins in Tuscany, Italy. Surface passivation may be less significant during carbonation of alkaline industrial wastes, however, which tend to be fine-grained. The grain size of mine tailings, for example, typically falls in the size range of the very fine and fine brucite employed in the experiments (e.g., Power et al., 2011). The passivating

effects of other Mg-carbonates than formed in this study (e.g., hydromagnesite, dypingite) may differ, and requires further investigation. The availability and distribution of water will play an important role controlling both the rate and extent of carbonation of mine tailings (Assima et al., 2013a), and other near surface mineral carbonation strategies that involve reaction in porous media such as engineered urban soils (Renforth et al., 2009; Washbourne et al., 2012). Low water contents will inhibit dissolution-precipitation processes, while high water content may effectively block gas transport (e.g., Collin and Rasmuson, 1988), promoting the development of preferential flow paths and reducing efficiency. If gaseous $CO_2$ were supplied to variably saturated porous media to enhance carbonation (Harrison et al., 2013b; Harrison et al., 2013a; Wilson et al., 2014), higher water contents would require greater pressure to maintain gas flow, increasing energy costs (Fig. 9). The consumption of water as reaction progresses may also provide an interesting feedback on the relative permeability of the porous media; an area that requires further study.

**Acknowledgements**

This research was funded by Carbon Management Canada National Centre of Excellence grants to GMD and KUM, and a Natural Sciences and Engineering Research Council of Canada (NSERC) Discovery Grant to GMD. Research by ALH was supported by a University of British Columbia Four Year fellowship and an NSERC postgraduate doctoral fellowship, and research by IMP was supported by an NSERC postdoctoral fellowship. We thank Timothy Mah, Maureen Soon, and Jenny Lai for their analytical assistance, and Jenine McCutcheon and Gordon Southam for providing XRF

measurements. We thank H. Hellevang, O. Sissmann, and an anonymous reviewer for insightful comments that significantly improved this manuscript, and B. Jamtveit for editorial handling. We appreciate the advice of Mati Raudsepp and Sasha Wilson regarding mineralogy, and of Mark Johnson and David Jones regarding instrumentation and datalogging. This is publication XXX of the Mineral Deposit Research Unit.

**References**

Andreani M., Luquot L., Gouze P., Godard M., Hoisé E. and Gibert B. (2009) Experimental study of carbon sequestration reactions controlled by the percolation of $CO_2$-rich brine through peridotites. *Environ. Sci. Technol.* **43**, 1226–1231.

Appelo C. and Postma D. (2005) *Geochemistry, Groundwater, and Pollution*. 2nd ed., CRC Press, Amsterdam.

Assima G. P., Larachi F., Beaudoin G. and Molson J. (2013a) Dynamics of carbon dioxide uptake in chrysotile mining residues – Effect of mineralogy and liquid saturation. *Int. J. Greenhouse Gas Control* **12**, 124–135.

Assima G. P., Larachi F., Molson J. and Beaudoin G. (2013b) Accurate and direct quantification of native brucite in serpentine ores – New methodology and implications for $CO_2$ sequestration by mining residues. *Thermochim. Acta* **566**, 281–291.

Assima G. P., Larachi F., Molson J. and Beaudoin G. (2014) Comparative study of five Québec ultramafic mining residues for use in direct ambient carbon dioxide mineral sequestration. *Chem. Eng. J.* **245**, 56–64.

Bear J. (1972) *Dynamics of fluids in porous media*. Elsevier, New York.

Béarat H., McKelvy M. J., Chizmeshya A. V. G., Gormley D., Nunez R., Carpenter R. W., Squires K. and Wolf G. H. (2006) Carbon sequestration via aqueous olivine mineral carbonation: Role of passivating layer formation. *Environ. Sci. Technol.* **40**, 4802–4808.

Beinlich A. and Austrheim H. (2012) In situ sequestration of atmospheric $CO_2$ at low temperature and surface cracking of serpentinized peridotite in mine shafts. *Chem. Geol.* **332-333**, 32–44.

Bish D. L., William Carey J., Vaniman D. T. and Chipera S. J. (2003) Stability of hydrous minerals on the martian surface. *Icarus* **164**, 96–103.

Bobicki E. R., Liu Q., Xu Z. and Zeng H. (2012) Carbon capture and storage using alkaline industrial wastes. *Prog. Energy Combust. Sci.* **38**, 302–320.

Boschi C., Dini A., Dallai L., Ruggieri G. and Gianelli G. (2009) Enhanced $CO_2$-mineral sequestration by cyclic hydraulic fracturing and Si-rich fluid infiltration into serpentinites at Malentrata (Tuscany, Italy). *Chem. Geol.* **265**, 209–226.

Brantley S. L. and Mellot N. P. (2000) Surface area and porosity of primary silicate minerals. *Am. Mineral.* **85**, 1767–1783.

Collin M. and Rasmuson A. (1988) A Comparison of Gas Diffusivity Models for Unsaturated Porous Media. *Soil Sci. Soc. Am. J.* **52**, 1559–1565.

Cubillas P., Köhler S., Prieto M., Causserand C. and Oelkers E. H. (2005) How do mineral coatings affect dissolution rates? An experimental study of coupled $CaCO_3$ dissolution—$CdCO_3$ precipitation. *Geochim. Cosmochim. Acta* **69**, 5459–5476.

Daval D., Martinez I., Corvisier J., Findling N., Goffé B. and Guyot F. (2009a) Carbonation of Ca-bearing silicates, the case of wollastonite: Experimental investigations and kinetic modeling. *Chem. Geol.* **265**, 63–78.

Daval D., Martinez I., Guigner J.-M., Hellmann R., Corvisier J., Findling N., Dominici C., Goffe B. and Guyot F. (2009b) Mechanism of wollastonite carbonation deduced from micro- to nanometer length scale observations. *Am. Mineral.* **94**, 1707–1726.

Daval D., Sissmann O., Menguy N., Saldi G. D., Guyot F., Martinez I., Corvisier J., Garcia B., Machouk I., Knauss K. G. and Hellmann R. (2011) Influence of amorphous silica layer formation on the dissolution rate of olivine at 90°C and elevated $pCO_2$. *Chem. Geol.* **284**, 193–209.

Felmy A. R., Qafoku O., Arey B. W., Hu J. Z., Hu M., Todd Schaef H., Ilton E. S., Hess N. J., Pearce C. I., Feng J. and Rosso K. M. (2012) Reaction of water-saturated supercritical $CO_2$ with forsterite: Evidence for magnesite formation at low temperatures. *Geochim. Cosmochim. Acta* **91**, 271–282.

Ferrini V., De Vito C. and Mignardi S. (2009) Synthesis of nesquehonite by reaction of gaseous $CO_2$ with Mg chloride solution: Its potential role in the sequestration of carbon dioxide. *J. Hazard. Mater.* **168**, 832–837.

Fredlund D. and Rahardjo H. (1993) *Soil mechanics for unsaturated soils*. John Wiley & Sons, Inc., New York.

Galeczka I., Wolff-Boenisch D., Oelkers E. H. and Gislason S. R. (2014) An experimental study of basaltic glass–$H_2O$–$CO_2$ interaction at 22 and 50°C: Implications for subsurface storage of $CO_2$. *Geochim. Cosmochim. Acta* **126**, 123–145.

Gautier J.-M., Oelkers E. H. and Schott J. (2001) Are quartz dissolution rates proportional to B.E.T. surface areas? *Geochim. Cosmochim. Acta* **65**, 1059–1070.

Gautier Q., Bénézeth P., Mavromatis V. and Schott J. (2014) Hydromagnesite solubility product and growth kinetics in aqueous solution from 25 to 75°C. *Geochim. Cosmochim. Acta*., doi: 10.1016/j.gca.2014.03.044

Gerdemann S. J., O'Connor W. K., Dahlin D. C., Penner L. R. and Rush H. (2007) Ex situ aqueous mineral carbonation. *Environ. Sci. Technol.* **41**, 2587–2593.

Gislason S. R. and Oelkers E. H. (2014) Geochemistry. Carbon storage in basalt. *Science* **344**, 373–374.

Gislason S. R., Wolff-Boenisch D., Stefansson A., Oelkers E. H., Gunnlaugsson E., Sigurdardottir H., Sigfusson B., Broecker W. S., Matter J. M. and Stute M. (2010)

Mineral sequestration of carbon dioxide in basalt: A pre-injection overview of the CarbFix project. *Int. J. Greenhouse Gas Control* **4**, 537–545.

Gualtieri A. F. (2000) Accuracy of XRPD QPA using the combined Rietveld ± RIR method research papers. *J. Appl. Crystallogr.* **33**, 267–278.

Hänchen M., Prigiobbe V., Baciocchi R. and Mazzotti M. (2008) Precipitation in the Mg-carbonate system—effects of temperature and $CO_2$ pressure. *Chem. Eng. Sci.* **63**, 1012–1028.

Harrison A. L., Power I. M. and Dipple G. M. (2013a) Accelerated carbonation of brucite in mine tailings for carbon sequestration. *Environ. Sci. Technol.* **47**, 126–134.

Harrison A. L., Power I. M. and Dipple G. M. (2013b) Strategies for enhancing carbon sequestration in Mg-rich mine tailings. In *Reliable Mine Water Technology (Vol. 1)* (eds. A. Brown, L. Figueroa, and C. Wolkersdorfer). Publication Printers, Denver, Colorado, USA. pp. 593–598.

Helgeson H. C., Murphy W. M. and Aagaard P. (1984) Thermodynamic and kinetic constraints on reaction rates among minerals and aqueous solutions. II. Rate constants, effective surface area, and the hydrolysis of feldspar. *Geochim. Cosmochim. Acta* **48**, 2405–2432.

Hellevang H., Pham V. T. H. and Aagaard P. (2013) Kinetic modelling of $CO_2$–water–rock interactions. *Int. J. Greenh. Gas Control* **15**, 3–15.

Hodson M. E. (2003) The influence of Fe-rich coatings on the dissolution of anorthite at pH 2.6. *Geochim. Cosmochim. Acta* **67**, 3355–3363.

Hövelmann J., Austrheim H. and Jamtveit B. (2012a) Microstructure and porosity evolution during experimental carbonation of a natural peridotite. *Chem. Geol.* **334**, 254–265.

Hövelmann J., Putnis C. V, Ruiz-Agudo E. and Austrheim H. (2012b) Direct nanoscale observations of $CO_2$ sequestration during brucite [$Mg(OH)_2$] dissolution. *Environ. Sci. Technol.* **46**, 5253–5260.

Huntzinger D. N., Gierke J. S., Kawatra S. K., Eisele T. C. and Sutter L. L. (2009) Carbon dioxide sequestration in cement kiln dust through mineral carbonation. *Environ. Sci. Technol.* **43**, 1986–92.

Jo H. Y., Ahn J.-H. and Jo H. (2012) Evaluation of the $CO_2$ sequestration capacity for coal fly ash using a flow-through column reactor under ambient conditions. *J. Hazard. Mater.* **241-242**, 127–136.

Johnson N. C., Thomas B., Maher K., Rosenbauer R. J., Bird D. and Brown G. E. (2014) Olivine dissolution and carbonation under conditions relevant for in situ carbon storage. *Chem. Geol.* **373**, 93–105.

Kelemen P. B. and Matter J. (2008) In situ carbonation of peridotite for $CO_2$ storage. *PNAS* **105**, 17295–17300.

King H. E., Plümper O. and Putnis A. (2010) Effects of secondary phase formation on the carbonation of olivine. *Environ. Sci. Technol.* **44**, 6503–6509.

Lackner K. S. (2003) A Guide to $CO_2$ Sequestration. *Science* **300**, 1677–1678.

Lackner K. S., Butt D. P. and Wendt C. H. (1997) Progress on binding $CO_2$ in mineral substrates. *Energy Convers. Manage.* **38**, S259–S264.

Lackner K. S., Wendt C. H., Butt D. P., Joyce E. L. and Sharp D. H. (1995) Carbon dioxide disposal in carbonate minerals. *Energy* **20**, 1153–1170.

Lafay R., Montes-Hernandez G., Janots E., Chiriac R., Findling N. and Toche F. (2014) Simultaneous precipitation of magnesite and lizardite from hydrothermal alteration of olivine under high-carbonate alkalinity. *Chem. Geol.* **368**, 63–75.

Lekakh S. N., Rawlins C. H., Robertson D. G. C., Richards V. L. and Peaslee K. D. (2008) Kinetics of aqueous leaching and carbonization of steelmaking slag. *Metall. Mater. Trans. B* **39**, 125–134.

Lichtner P. (1996) Continuum formulation of multicomponent-multiphase reactive transport. *Rev. Mineral. Geochem.* **34**, 1996.

Loring J. S., Thompson C. J., Wang Z., Joly A. G., Sklarew D. S., Schaef H. T., Ilton E. S., Rosso K. M. and Felmy A. R. (2011) In situ infrared spectroscopic study of forsterite carbonation in wet supercritical $CO_2$. *Environ. Sci. Technol.* **45**, 6204–10.

Luttge A. and Arvidson R. S. (2008) The mineral-water interface. In *Kinetics of water-rock interaction* (eds. S. L. Brantley, J. D. Kubicki, and A. F. White). Springer, New York. pp. 73–107.

Mason E. A. and Malinauskas A. P. (1983) Gas transport in porous media: The Dusty-Gas Model. *Chem. Eng. Monogr.*, vol. 17, Elsevier, New York.

Mayer K. U., Frind E. O. and Blowes D. W. (2002) Multicomponent reactive transport modeling in variably saturated porous media using a generalized formulation for kinetically controlled reactions. *Water Resour. Res.* **38**, 1174.

McGrail B. P., Schaef H. T., Ho A. M., Chien Y.-J., Dooley J. J. and Davidson C. L. (2006) Potential for carbon dioxide sequestration in flood basalts. *J. Geophys. Res.* **111**, B12201.

Miller Q. R. S., Thompson C. J., Loring J. S., Windisch C. F., Bowden M. E., Hoyt D. W., Hu J. Z., Arey B. W., Rosso K. M. and Schaef H. T. (2013) Insights into silicate carbonation processes in water-bearing supercritical $CO_2$ fluids. *Int. J. Greenh. Gas Control* **15**, 104–118.

Molins S. and Mayer K. U. (2007) Coupling between geochemical reactions and multicomponent gas and solute transport in unsaturated media: A reactive transport modeling study. *Water Resour. Res.* **43**, 1–16.

Montes-Hernandez G., Chiriac R., Toche F. and Renard F. (2012) Gas-solid carbonation of $Ca(OH)_2$ and CaO particles under non-isothermal and isothermal conditions by using a thermogravimetric analyzer: Implications for $CO_2$ capture. *Int. J. Greenhouse Gas Control* **11**, 172–180.

Navarre-Sitchler A., Steefel C. I., Sak P. B. and Brantley S. L. (2011) A reactive-transport model for weathering rind formation on basalt. *Geochim. Cosmochim. Acta* **75**, 7644–7667.

Nicholson R. V., Gillham R. W. and Reardon E. J. (1990) Pyrite oxidation in carbonate-buffered solution: 2. Rate control by oxide coatings. *Geochim. Cosmochim. Acta* **54**, 395–402.

Oskierski H. C., Dlugogorski B. Z. and Jacobsen G. (2013) Sequestration of atmospheric $CO_2$ in chrysotile mine tailings of the Woodsreef Asbestos Mine, Australia: Quantitative mineralogy, isotopic fingerprinting and carbonation rates. *Chem. Geol.* **358**, 156–169.

Park A. A. and Fan L. (2004) $CO_2$ mineral sequestration: Physically activated dissolution of serpentine and pH swing process. *Chem. Eng. Sci.* **59**, 5241–5247.

Paukert A. N., Matter J. M., Kelemen P. B., Shock E. L. and Havig J. R. (2012) Reaction path modeling of enhanced *in situ* $CO_2$ mineralization for carbon sequestration in the peridotite of the Samail Ophiolite, Sultanate of Oman. *Chem. Geol.* **330-331**, 86–100.

Petrovich R. (1981) Kinetics of dissolution of mechanically comminuted rock-forming oxides and silicates-I . Deformation and dissolution of quartz under laboratory conditions. *Geochim. Cosmochim. Acta* **45**, 1665.

Van Pham T. H., Aagaard P. and Hellevang H. (2012) On the potential for $CO_2$ mineral storage in continental flood basalts - PHREEQC batch- and 1D diffusion-reaction simulations. *Geochem. Trans.* **13**, 5.

Pham V. T. H., Lu P., Aagaard P., Zhu C. and Hellevang H. (2011) On the potential of $CO_2$–water–rock interactions for $CO_2$ storage using a modified kinetic model. *Int. J. Greenhouse Gas Control* **5**, 1002–1015.

Pokrovsky O. S., Schott J. and Castillo A. (2005) Kinetics of brucite dissolution at 25°C in the presence of organic and inorganic ligands and divalent metals. *Geochim. Cosmochim. Acta* **69**, 905–918.

Pokrovsky O. and Schott J. (2004) Experimental study of brucite dissolution and precipitation in aqueous solutions: Surface speciation and chemical affinity control. *Geochim. Cosmochim. Acta* **68**, 31–45.

Pokrovsky O. and Schott J. (2000) Kinetics and mechanism of forsterite dissolution at 25°C and pH from 1 to 12. *Geochim. Cosmochim. Acta* **64**, 3313–3325.

Power I. M., Harrison A. L., Dipple G. M. and Southam G. (2013b) Carbon sequestration via carbonic anhydrase facilitated magnesium carbonate precipitation. *Int. J. Greenh. Gas Control* **16**, 145–155.

Power I. M., Harrison A. L., Dipple G. M., Wilson S. A., Kelemen P. B., Hitch M. and Southam G. (2013a) Carbon Mineralization: From Natural Analogues to Engineered Systems. *Rev. Mineral. Geochem.* **77**, 305–360.

Power I. M., McCutcheon J., Harrison A. L., Wilson S. A., Dipple G. M., Kelly S., Southam C. and Southam G. (2014a) Strategizing carbon-neutral mines: A case for pilot projects. *Minerals.* **4**, 399–436.

Power I. M., Wilson S. A., Harrison A. L., Dipple G. M., Mccutcheon J., Southam G. and Kenward P. A. (2014b) A depositional model for hydromagnesite-magnesite playas near Atlin, British Columbia, Canada. *Sedimentology*, doi: 10.1111/sed.12124

Power I. M., Wilson S. A., Small D. P., Dipple G. M., Wan W. and Southam G. (2011) Microbially mediated mineral carbonation: Roles of phototrophy and heterotrophy. *Environ. Sci. Technol.* **45**, 9061–9068.

Power I. M., Wilson S. A., Thom J. M., Dipple G. M., Gabites J. E. and Southam G. (2009) The hydromagnesite playas of Atlin, British Columbia, Canada: A biogeochemical model for $CO_2$ sequestration. *Chem. Geol.* **260**, 286–300.

Power I. M., Wilson S. A., Thom J. M., Dipple G. M. and Southam G. (2007) Biologically induced mineralization of dypingite by cyanobacteria from an alkaline wetland near Atlin, British Columbia, Canada. *Geochem. Trans.* **8**, 13.

Pronost J., Beaudoin G., Lemieux J.-M., Hebert R., Constantin M., Marcouiller S., Klein M., Duchesne J., Molson J. W., Larachi F. and Maldague X. (2012) $CO_2$-depleted warm air venting from chrysotile milling waste (Thetford Mines, Canada): Evidence for in-situ carbon capture from the atmosphere. *Geology* **40**, 275–278.

Pronost J., Beaudoin G., Tremblay J. and Constantin M. (2011) Carbon sequestration kinetic and storage capacity of ultramafic mining waste. *Environ. Sci. Technol.* **45**, 9413–9420.

Renforth P., Manning D. A. C. and Lopez-Capel E. (2009) Carbonate precipitation in artificial soils as a sink for atmospheric carbon dioxide. *Appl. Geochemistry* **24**, 1757–1764.

Rigby M. and Prausnitz J. M. (1967) Solubility of water in compressed nitrogen, argon, and methane. *J. Phys. Chem.* **72**, 330–334.

Saldi G. D., Daval D., Morvan G. and Knausss K. G. (2013) The role of Fe and redox conditions in olivine carbonation rates: An experimental study of the rate limiting reactions at 90 and 150°C in open and closed systems . *Geochim. Cosmochim. Acta* **118**, 157–183.

Schaef H. T., McGrail B. P., Loring J. L., Bowden M. E., Arey B. W. and Rosso K. M. (2013) Forsterite [$Mg_2SiO_4$] Carbonation in wet supercritical $CO_2$: An in situ High-Pressure X-ray Diffraction Study. *Environ. Sci. Technol.* **47**, 174–181.

Schaef H. T., Windisch C. F., McGrail B. P., Martin P. F. and Rosso K. M. (2011) Brucite [$Mg(OH_2)$] carbonation in wet supercritical $CO_2$: An *in situ* high pressure X-ray diffraction study. *Geochim. Cosmochim. Acta* **75**, 7458–7471.

Seifritz W. (1990) $CO_2$ disposal by means of silicates. *Nature* **345**, 486.

Sissmann O., Brunet F., Martinez I., Guyot F., Verlaguet A., Pinquier Y. and Daval D. (2014) Enhanced olivine carbonation within a basalt as compared to single-phase experiments: Reevaluating the potential of $CO_2$ mineral sequestration. *Environ. Sci. Technol.* **48**, 5512–5519.

Sissmann O., Daval D., Brunet F., Guyot F., Verlaguet A., Pinquier Y., Findling N. and Martinez I. (2013) The deleterious effect of secondary phases on olivine carbonation yield: Insight from time-resolved aqueous-fluid sampling and FIB-TEM characterization. *Geochim. Cosmochim. Acta* **357**, 186–202.

Steefel C. I. and Van Cappellen P. (1990) A new kinetic approach to modeling water-rock interaction: The role of nucleation, precursors, and Ostwald ripening. *Geochim. Cosmochim. Acta* **54**, 2657–2677.

Stockmann G. J., Wolff-Boenisch D., Bovet N., Gislason S. R. and Oelkers E. H. (2014) The role of silicate surfaces on calcite precipitation kinetics. *Geochim. Cosmochim. Acta* **135**, 231–250.

Stockmann G. J., Wolff-Boenisch D., Gislason S. R. and Oelkers E. H. (2011) Do carbonate precipitates affect dissolution kinetics? 1: Basaltic glass. *Chem. Geol.* **284**, 306–316.

Stockmann G. J., Wolff-Boenisch D., Gislason S. R. and Oelkers E. H. (2013) Do carbonate precipitates affect dissolution kinetics? 2. Diopside. *Chem. Geol.* **337-338**, 56–66.

Velbel M. A. (1993) Formation of protective surface layers during silicate-mineral weathering under well-leached, oxidizing conditions. *Am. Mineral.* **78**, 405–414.

Wanner C., Eggenberger U. and Mäder U. (2011) Reactive transport modelling of Cr(VI) treatment by cast iron under fast flow conditions. *Appl. Geochem.* **26**, 1513–1523.

Washbourne C.-L., Renforth P. and Manning D. A. C. (2012) Investigating carbonate formation in urban soils as a method for capture and storage of atmospheric carbon. *Sci. Total Environ.* **431**, 166–175.

White A. F. and Brantley S. L. (2003) The effect of time on the weathering of silicate minerals: Why do weathering rates differ in the laboratory and field? *Chem. Geol.* **202**, 479–506.

Wilson S. A., Barker S. L. L., Dipple G. M. and Atudorei V. (2010) Isotopic disequilibrium during uptake of atmospheric $CO_2$ into mine process waters: Implications for $CO_2$ sequestration. *Environ. Sci. Technol.* **44**, 9522–9529.

Wilson S. A. and Bish D. L. (2012) Stability of Mg-sulfate minerals in the presence of smectites: Possible mineralogical controls on $H_2O$ cycling and biomarker preservation on Mars. *Geochim. Cosmochim. Acta* **96**, 120–133.

Wilson S. A., Dipple G. M., Power I. M., Thom J. M., Anderson R. G., Raudsepp M., Gabites J. E. and Southam G. (2009) Carbon dioxide fixation within mine wastes of ultramafic-hosted ore deposits: Examples from the Clinton Creek and Cassiar chrysotile deposits, Canada. *Econ. Geol.* **104**, 95–112.

Wilson, S.A., Harrison, A.L., Dipple, G.M., Power, I.M., Barker, S.L.L., Mayer, K.U., Fallon, S.J., Raudsepp, M., Southam, G. (2014) Offsetting of $CO_2$ emissions by air capture in mine tailings at the Mount Keith Nickel Mine, Western Australia: Rates, controls and prospects for carbon neutral mining. *Int. J. Greenh. Gas Control* **25**, 121–140.

**Figure Captions**

**Figure 1.** Schematic of experimental setup.

**Figure 2.** Mineral abundance profiles determined using Rietveld refinement of X-ray diffraction data for 35% saturated columns with very fine (a), fine (b), and medium (c) brucite. Data are from six samples for the very fine and fine brucite columns, and seven samples for the medium brucite column taken with depth over ~2 cm intervals. Each of these was a bulk, homogenized sample of the entire depth interval. The black shaded, dotted, and diagonally striped areas represent the abundance of brucite, the poorly crystalline flakey Mg-carbonate phase, and nesquehonite, respectively. Lines with symbols represent the abundance of $CO_2$ by mass in the solid material with depth as determined using $\%CO_2$ measurements. $\%CO_2$ data from the 35% saturated column using brucite that was rinsed to remove the surface powder is plotted with a blue line and filled square data points in (c). Dashed lines represent MIN3P-DUSTY output for the abundance of $CO_2$ by mass in the solid phase for each grain size using the threshold function. $CO_2$ was supplied at the base.

**Figure 3.** Mineral abundance profiles determined using Rietveld refinement of X-ray diffraction data for columns containing medium brucite at 15% (a), 35% (b), and 50% (c) water saturation. Data are from six samples for the 15% saturated column, and seven samples for the 35% and 50% saturated columns taken with depth over ~2 cm intervals, except for the base sample from the 15% saturated column, which was 4 cm. Each of these was a bulk, homogenized sample of the entire depth interval. The black shaded,

dotted, and diagonally striped areas represent the abundance of brucite, the poorly crystalline flakey Mg-carbonate phase, and nesquehonite, respectively. Lines with symbols represent the abundance of $CO_2$ by mass in the solid phase with depth as determined using $\%CO_2$ measurements. $\%CO_2$ data from the 35% saturated column using brucite that was rinsed to remove the surface powder is plotted with a blue line and filled square data points in (b). Dashed lines represent MIN3P-DUSTY output for the abundance of $CO_2$ by mass in the solid phase for each grain size using the threshold function. $CO_2$ was supplied at the base.

**Figure 4.** Mass of $CO_2$ sequestered versus time calculated based on the column mass gain over time (a). Instantaneous carbonation rate versus time in 35% saturated columns containing very fine, fine, and medium brucite (b). Instantaneous carbonation rate versus time in columns containing medium brucite at 15%, 35%, and 50% water saturation (c). Square symbols represent columns at 35% saturation, triangles are 50% saturation, and circles are 15% saturation. Grain size for columns of the same water saturation are distinguished by colour, whereas all columns with medium brucite are represented by various shades of green. Open symbols represent duplicate experiments, and diamonds represent the mass of $CO_2$ sequestered calculated using $\%CO_2$ measurements. '*SX*' labels indicate reaction stages 1-4.

**Figure 5.** $CO_2$ breakthrough curves measured at column outlets versus time and MIN3P-DUSTY modelling results for 35% saturated columns containing very fine (a), fine (b), and medium brucite (c), and columns containing medium brucite with 50% water saturation (d). $CO_2$ breakthrough data were unavailable for 15% saturated medium brucite

columns. $CO_2$ breakthrough curves are expressed as '$C/C_0$', where C is the $CO_2$ concentration of the gas effluent at a given time, and $C_0$ is the $CO_2$ concentration of the effluent following the carbonation reaction. Solid black, red, and green lines represent experimental data from the very fine, fine, and medium 35% and 50% saturated columns, respectively. Dashed and solid blue lines represent MIN3P-DUSTY output from simulations employing the geometric and threshold models, respectively. '*SX*' labels indicate reaction stages 1-4.

**Figure 6.** Scanning electron micrographs of initial and reacted material. Initial medium brucite (brc) showing brucite powder on the surface of large grains (a). Reaction products from the 35% saturated medium brucite column showing nesquehonite (nsq) surrounding unreacted brucite, a lesser extent of precipitates surrounding quartz (qtz), and some edges of brucite that are not coated by carbonate precipitates (b). Micrograph showing a coating of the flakey, poorly crystalline secondary Mg-carbonate phase covering a brucite grain in a sample from the fine brucite column (c). The inset figure in 'c' displays a representative energy dispersive spectrum collected from the flakey phase. Micrograph of a sample from the very fine brucite column showing secondary carbonate infilling the space between quartz and remaining brucite grains, and cementing grains together (d). Micrographs of non-porous nesquehonite coating a 'medium' brucite grain from the 35% saturated column (e-f).

**Figure 7.** Conceptual diagram of the four reaction stages: stage 1) carbonation of fines, stage 2) reaction of the bulk of the brucite, stage 3) the majority of brucite is no longer available for reaction such that the reaction rate approaches zero, and stage 4) negligible

reaction. Areas shaded green represent brucite grains, grey represents flakey poorly crystalline Mg-carbonate, purple represents nesquehonite, and red indicates where the carbonation reaction is predominantly occurring during each stage.

**Figure 8.** Absolute carbonation rate (g $CO_2$ $h^{-1}$) for all 35% saturated columns of different grain size versus BET measured initial brucite surface area ($m^2$ $g^{-1}$) for each grain size. The medium brucite is indicated by the green square, the fine by the red square, and the very fine by the black square. The white square with the dashed line indicates the approximate carbonation rate that would be achieved for very fine brucite with a 5-fold greater $CO_2$ supply rate, as estimated using MIN3P-DUSTY. The grey dashed line indicates the approximate trend in carbonation rate with BET surface area if $CO_2$ supply were not limiting. The grey shaded region indicates the rate of $CO_2$ supply to the columns as estimated using the measured gas flow rate out of the very fine column with laboratory air flow only, and at the end of the experiment once the column ceased gaining mass.

**Figure 9.** The extent of brucite carbonation measured in this study and by Assima et al. (2013a) and the calculated percent reduction in gaseous $CO_2$ flux through a porous medium at a fixed pressure as a function of various degrees of water saturation. Circles represent data from 10-15% saturated experiments, squares represent 35% saturated experiments, triangles represent 50% saturated experiments, and diamonds represent 100% saturated experiments. The shaded region represents the approximate range of water saturation that may both optimize the extent of carbonation and minimize energy costs associated with increased $CO_2$ injection pressure were gaseous $CO_2$ supplied to a porous medium as part of an industrial $CO_2$ sequestration project (e.g., Wilson et al.,

2014). The experiments conducted by Assima et al. (2013a) investigated carbonation of chrysotile mining residues that contained brucite using 14 vol.% $CO_2$ with an experimental duration of 1 day. The carbonation extent of brucite was estimated assuming that 93% of the $CO_2$ sequestration recorded was due to brucite carbonation (after Assima et al., 2013a). The $CO_2$ flux was calculated using Darcy's law for a 10 vol.% $CO_2$ gas mixture (balance $N_2$) at a constant pressure of 1 atm, assuming transport is dominated by advection (refer to the SM for details regarding the calculation).

Table 1. Summary of experimental conditions.

| | Experiment | Brucite particle diameter (µm) | Mean particle radius (µm) | Brucite surface area ($m^2$ $g^{-1}$) | Sediment height (cm) | Porosity | Volume water added (mL) | Saturation[a] (%) |
|---|---|---|---|---|---|---|---|---|
| **Grain size trial** | very fine | <53 | 12 | 5.2 | 12.3 | 0.49 | 58 | 35 |
| | fine | 53-180 | 39 | 3.7 | 12.3 | 0.49 | 58 | 35 |
| | medium | 250-500 | 188 | 2.4 | 13.7 | 0.54 | 71 | 35 |
| | | | | | | | | |
| **Saturation trial** | 15% | 250-500 | 188 | 2.4 | 13.2 | 0.53 | 29 | 15 |
| | 35% | 250-500 | 188 | 2.4 | 13.7 | 0.54 | 71 | 35 |
| | 50% | 250-500 | 188 | 2.4 | 13.4 | 0.53 | 97 | 50 |

[a]Saturation = (volume water/volume pore space) × 100%

Table 2. Summary of mass of $CO_2$ sequestered, carbonation rate, reaction stoichiometry, and extent of carbonation in experiments for which solids were analyzed.

| | | Total mass $CO_2$ sequestered (g) | | | | | | | |
|---|---|---|---|---|---|---|---|---|---|
| | **Experiment** | **Total inorganic carbon content data** | **Gravimetric data** | **Mass $CO_2$ in nsq[a] (g)** | **Mass solid phase $CO_2$ not stored in nsq (g)[b]** | **Mass $CO_2$ in flakey carbonate (g)[c]** | **Extent of carbonation (%)** | **Mg:$CO_2$ ratio** | **Carbonation rate (g $CO_2$ $h^{-1}$)[d]** |
| **Grain size trial** | very fine | 16.8 | 16.4 | 4.0 | 12.8 | 12.8 | 94 | 1.7 | 0.15 |
| | fine | 13.1 | 14.3 | 3.6 | 9.4 | 9.4 | 82 | 1.9 | 0.15 |
| | medium | 9.0 | 8.3 | 2.1 | 6.9 | 6.9 | 63 | 2.1 | 0.09 |
| | | | | | | | | | |
| **Saturation trial** | 15% | 5.2 | 4.4 | 0.7 | 4.5 | 4.5 | 41 | 2.4 | < 0.08 |
| | 35% | 9.0(9.3)[e] | 8.3(9.2)[e] | 2.1 | 6.9 | 6.9 | 63 | 2.1 | 0.09 |
| | 50% | 8.6 | 8.4 | 4.7 | 3.9 | 3.9 | 62 | 2.1 | 0.08 |

[a]nsq = nesquehonite
[b]Mass difference between total inorganic carbon content measurement and $CO_2$ stored in nsq
[c]Equated to mass of solid phase $CO_2$ not stored in nsq
[d]Average carbonation rate during stage 2
[e]Bracketed values are from the 35% saturated rinsed medium brucite column

$$r_{instant} = \frac{[m_2 - m_1]}{[t_2 - t_1]} \qquad \text{Equation 1}$$

$$r_{brc} = k^o_{eff}[HCO_3^-]^{0.56}(1 - \Omega^2) \qquad \text{Equation 2}$$

$$k^o_{eff} = k^0 SA \quad \text{Equation 3}$$

$$\frac{Mg}{C} = \frac{\left[n_{brc_i} - n_{brc_f}\right]}{\left[n_{CO_{2_f}} - n_{CO_{2_i}}\right]} \quad \text{Equation 4}$$

$$k^g_{eff} = (k^0 SA)\left(\frac{\varphi^t}{\varphi^0}\right)^{2/3} \qquad \text{Equation 5}$$

$$Mg(OH)_2 + CO_2 + 2H_2O \rightarrow MgCO_3 \cdot 3H_2O \qquad \text{Equation 6}$$

$$k_{eff}^{t} = (k^{0}SA)\left[1 - \left(\frac{\varphi^{0} - \varphi^{t}}{\varphi^{0} - \varphi^{p}}\right)^{n}\right] \qquad \text{Equation 7}$$

Figure 1



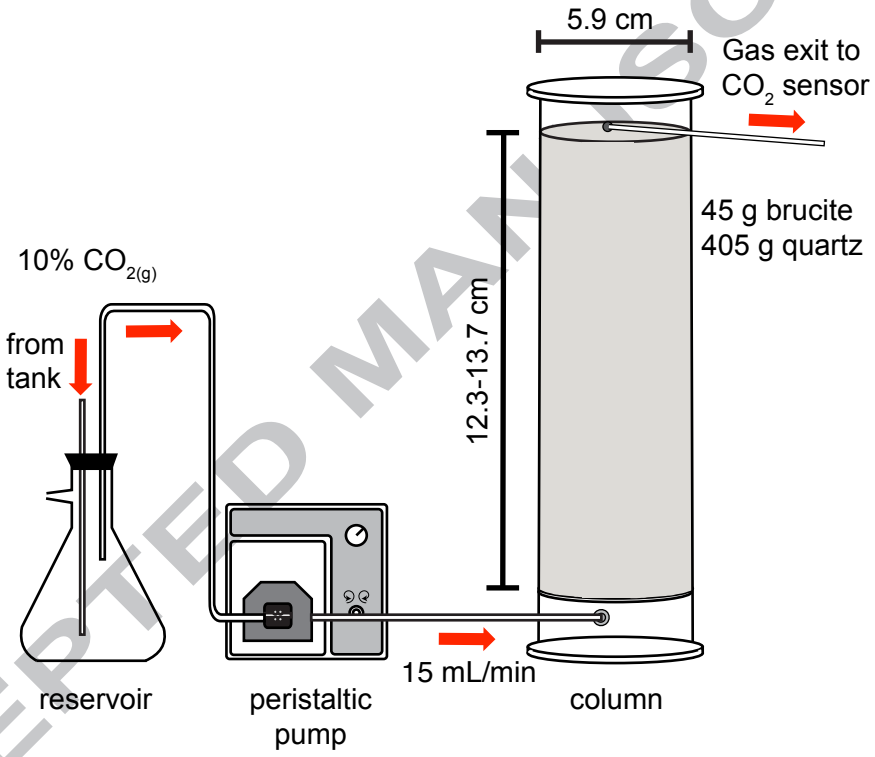

Figure 2



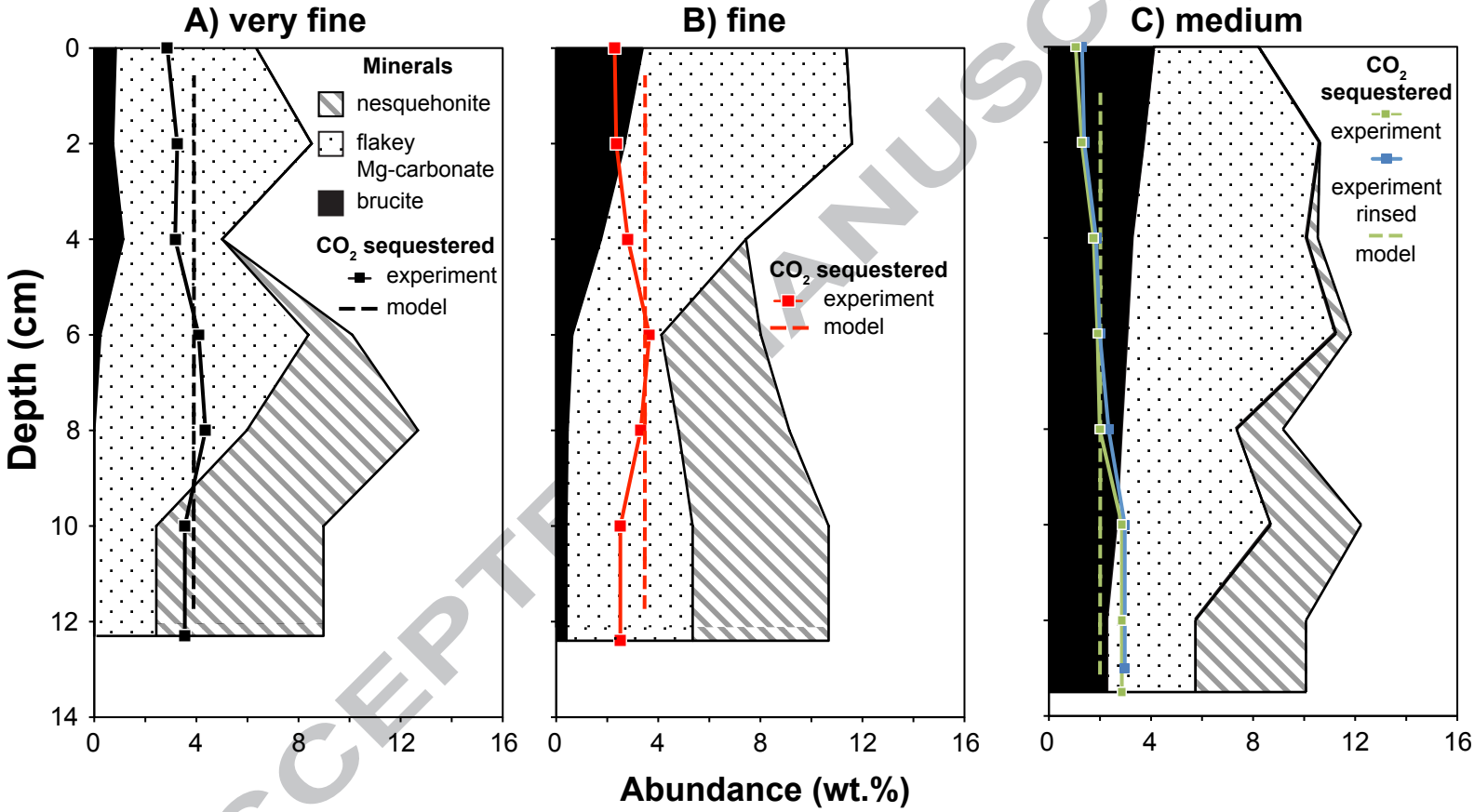

Figure 3



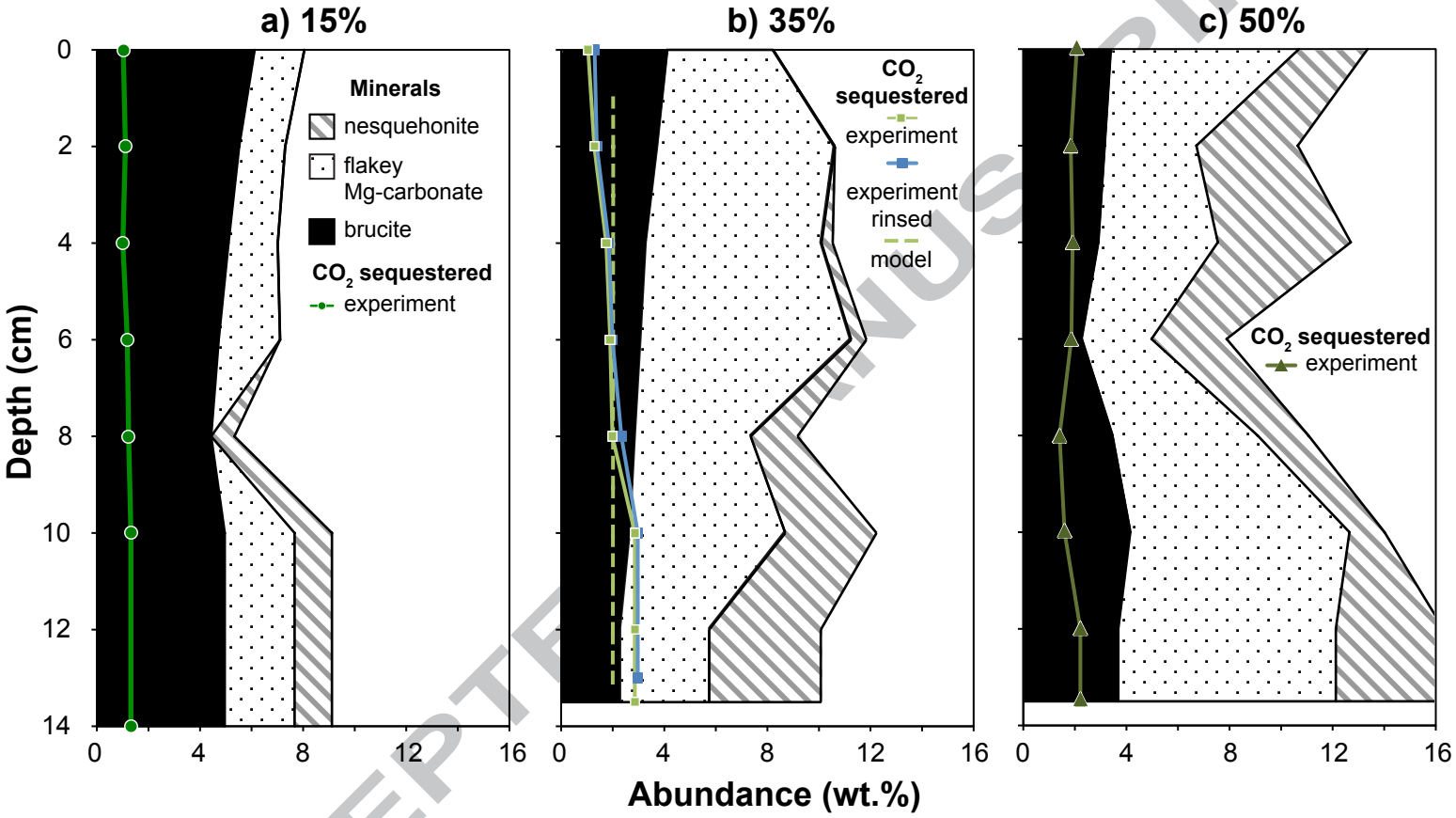

Figure 4



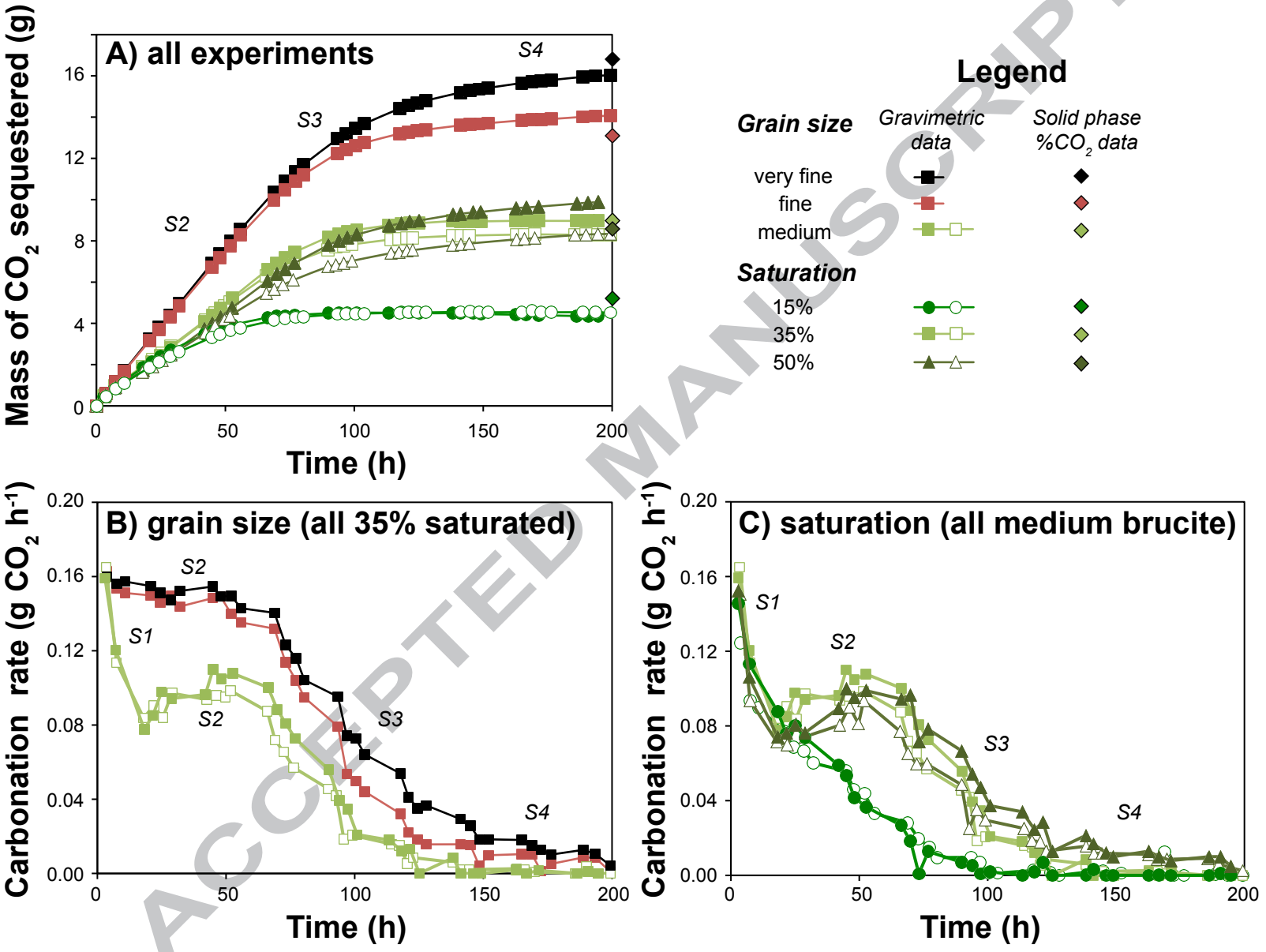

Figure 5



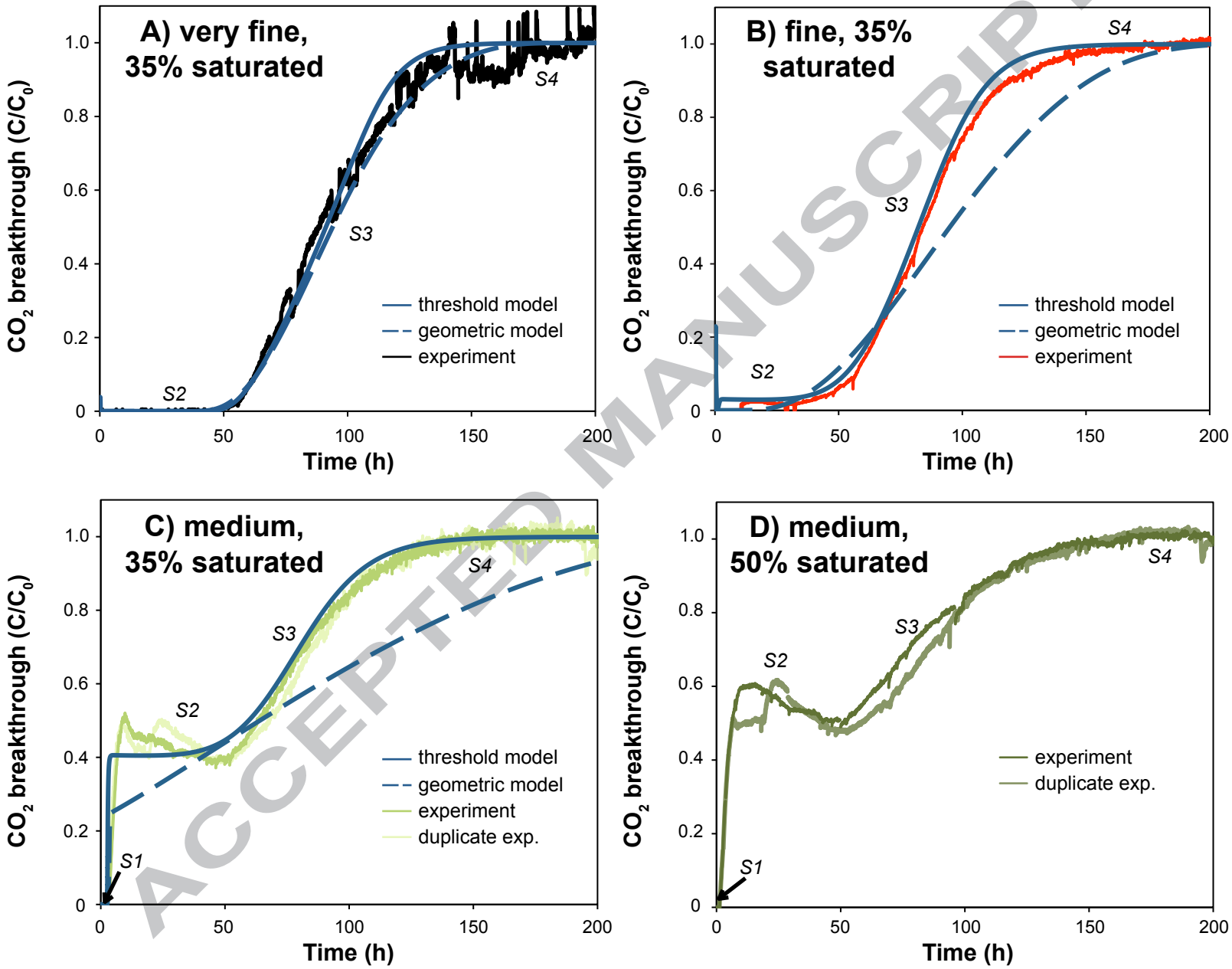

Figure 6



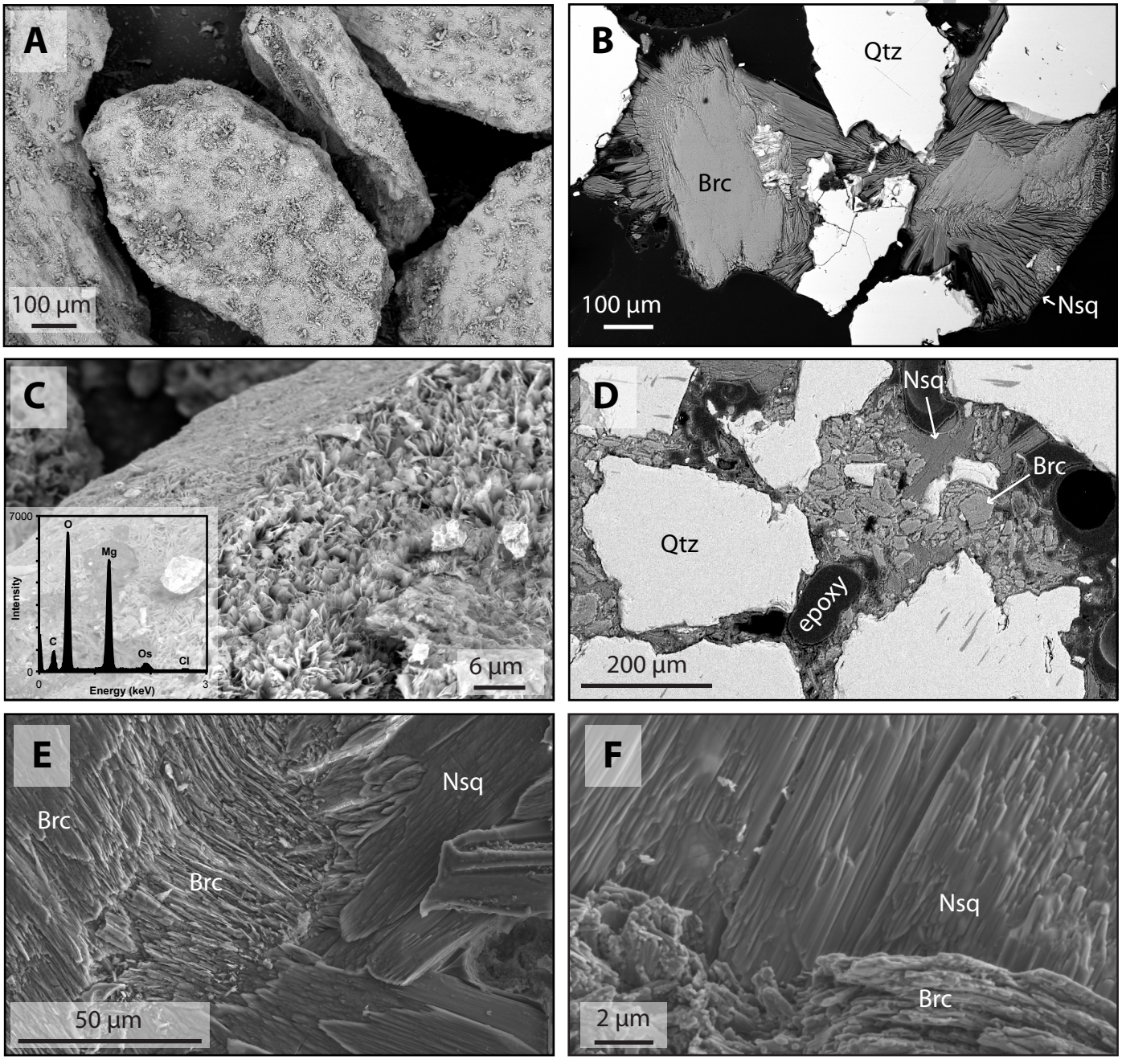

Figure 7



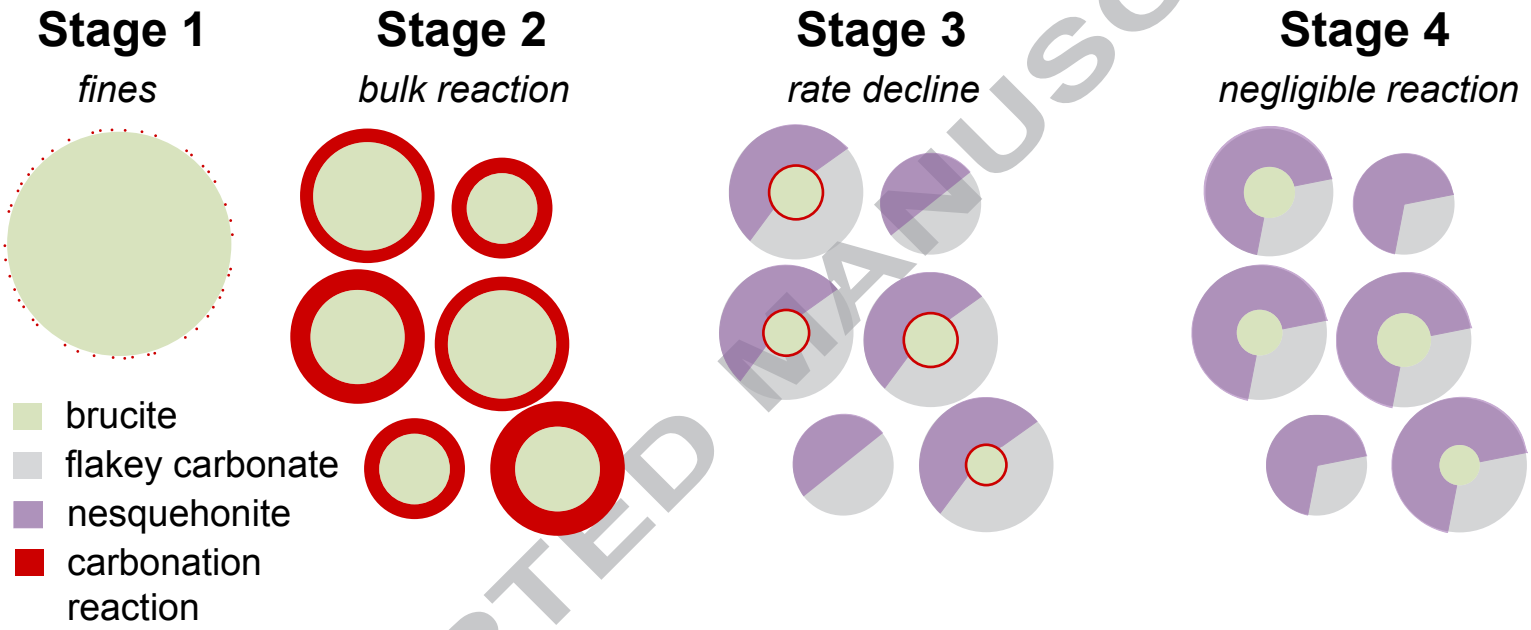

Figure 8



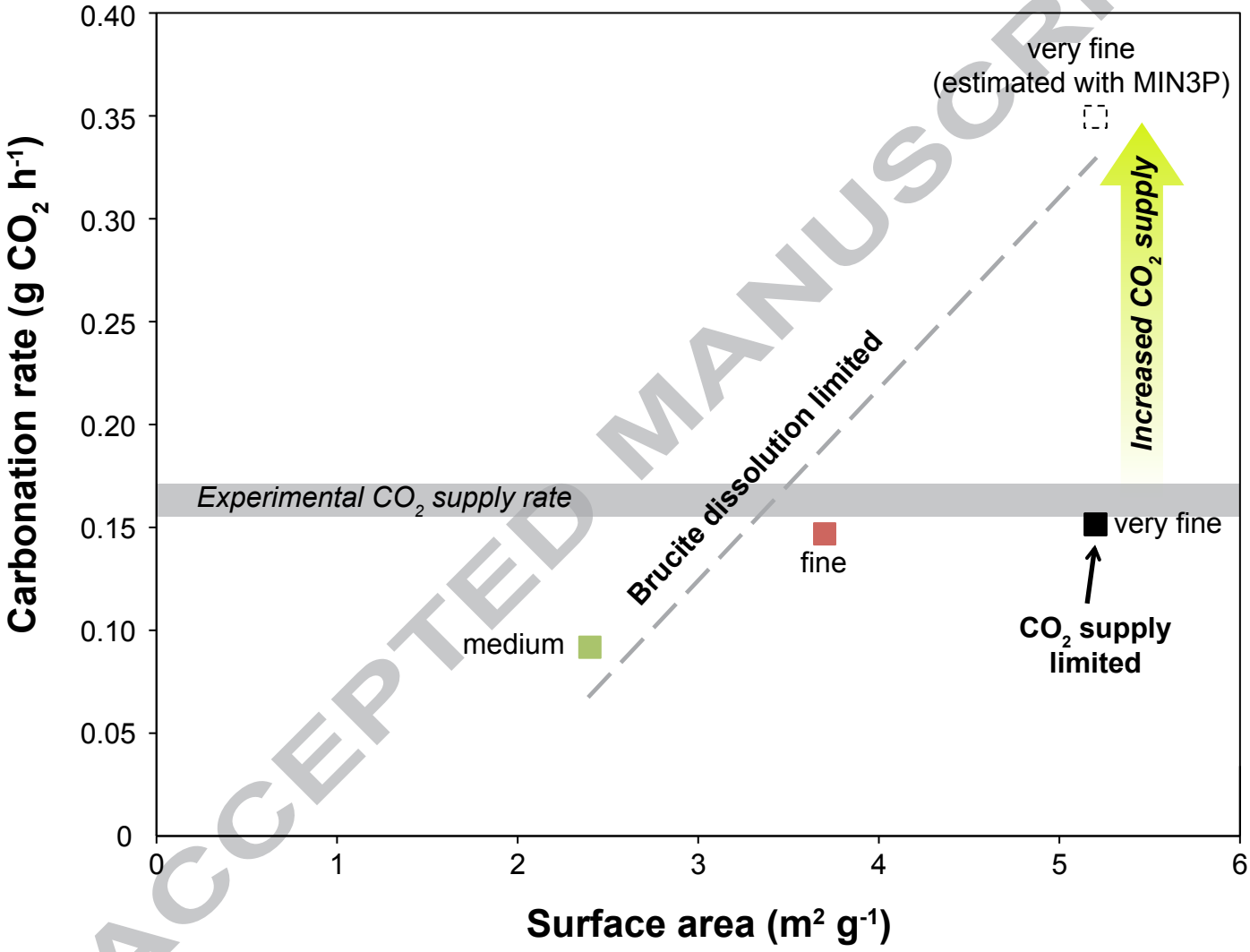

Figure 9